Bachelor Thesis

Graphene on Diamond

Luka Glomazic

Supervisors
Prof. Dr Jan Meijer
Dr Ralf Wunderlich

UNIVERSITÄT
LEIPZIG

Faculty of Physics and Earth Sciences
Felix Bloch Institute for Solid State Physics
Applied Quantum Systems
Universität Leipzig
Germany

January 18, 2021

Graphene on Diamond

Luka Glomazić

Abstract

Our primary objective was to determine the correlation between the nitrogen-vacancy centres implanted in a diamond substrate and a graphene layer deposited on top of the implantation spot using the principle of Förster resonance energy transfer. A diamond substrate was implanted with $^{14}N^{+}$ ions with different energies and doses. Graphene was deposited using a tape deposition method and the time-resolved fluorescence lifetime measurements were performed.

The data obtained from the measurements were analyzed using Python and OriginLab, fitted with mono- and bi-exponential decay functions. Overall, the observed results were questionable compared to the expectations for the fluorescence lifetime of the excited state of the two charge states of NV centres in the presence and in the absence of graphene. The observed lifetime of the NV0 centre in the absence of graphene was 21.516 ± 1.510 ns and in the presence of it, was 24.107 ± 2.227 ns. For the NV centre, the observed lifetimes in the absence and the presence of graphene were 3.848 ± 0.982 ns and 8.037 ± 1.077 ns. The results are inconsistent with the expectations, even contradictory since we expected to see a shortening in the lifetimes and not the increase.

This was a consequence of a few factors. The graphene deposited by tape was too thick, having twenty-one layers. The maximum laser power for the time-resolved fluorescence lifetime measurements was too weak and due to the graphene thickness, only about 60 % of the fluorescence intensity reached the detector. In the end, the results did not fulfil the requirement for the estimate of the Förster resonance energy transfer between the NV centres and graphene.

Statement of Authorship

I hereby certify that this bachelor thesis has been composed by myself and describes my own work, unless otherwise acknowledged in the test. All references and verbatim extracts have been quoted and all sources of information have been specifically acknowledged. It has not been accepted in any previous application for a degree.

Luka Glomazic

Signature

Leipzig, 18.01.2021

Date

Acknowledgements

First and foremost, I would like to thank my supervisor, Dr Ralf Wunderlich, for his kindness, his understanding and his willingness to answer each and every one of my many questions and for guiding me calmly through this process every step of the way.

I wish to express my deepest gratitude to Prof. Dr Jan Meijer for giving me the chance to do this work as a part of his research group and thus allowing me to pave my way towards further knowledge and broadening my vision. Special thanks to all members of the Applied Quantum Systems department for welcoming me with open hands and helping whenever it was needed.

I am indebted to M. Sc. Evgeny Krueger who helped me greatly in the final part of my work with the measurements and the analysis of time-resolved fluorescence lifetime, who showed great commitment and even stayed working overtime to help me get the best results possible.

I would like to thank the Academic Assistant, José Barzola Quiquia, for showing me the way in the very beginning of this work and teaching me the hardships of research, for providing the test samples and for answering even my most naive questions with full attention.

I would also like to thank B. Sc. Danica Pavićević who was irreplaceable support in the hardest of times, without who this whole work would have been much harder and much more stressful. Many thanks to all of my friends who were there for me in times of need.

Finally, I would like to thank my family for the endless support they showed and for believing in me every second of every day without slightest of doubt.

Contents

Chapter 1

Introduction

From 2004, when the first graphene layer was successfully isolated by the group of Andre Geim and Konstantin Novoselov[1, 2], who later got the Noble prize for this work, graphene has started a frenzy of extensive research on its remarkable properties. It was already a known topic for scientists, since it was first assumed as the highly lamellar structure of thermally reduced graphite oxide back in 1859 by Benjamin Collins Brodie[3] and later theoretically explored as a single layer by P. R. Wallace in 1947. However, the credit for its founding goes to Hanns-Peter Boehm[4] who introduced the term *graphene* in 1986.

Nowadays, graphene is considered to be one of the most prominent and prospective materials for a wide range of applications in all aspects of life. As a 2D, zero-gap, semi-metallic material formed by sp^2 carbon-carbon bonded honey comb lattice, many research groups have studied its potential use in material science, soft-matter physics and quantum technologies. For example graphene field-effect transistor (GFET)[5], graphene quantum dots (GQDs)[6], quantum computing with graphene plasmons[7] are some of the many reasearch topics in this category in recent years.

Another widely studied topic in scientific community in the past decades is the nitrogen-vacancy defect in diamond and its two charge states (negative NV^-, and electrically neutral NV^0) and their use as single-photon sources. These optical centers in diamond have been studied as hosts for quantum information processing[8, 11]. Diamond, as a great insulator with its wide band gap (5.47 eV) that can be turned into a semiconductor with appropriate doping, provides a great host for the study of such optical centers and their use as quantum qubits. However, it is not without difficulties that these results can be achieved. Actually, a deterministic generation of such centers is not possible yet.

Especially interesting for this work are the quantum applications of graphene layers and the NV defects, as the topic of this thesis is the attempt to determine the correlation of graphene and NV defects in diamond and its dependence on the distance between each other through the use of the properties of Förster resonance energy transfer. Fluorescence lifetime analysis of NV centers in the presence and absence of graphene is employed as the method to determine this coupling dependency.

Chapter two of this work focuses on the theoretical background of diamond, diamond defects and graphene, as well as the physical processes in the experimental procedure. It is the purpose of this chapter to explain all the relevant principles

affecting the experiment. Starting with diamond and graphene electronic and optical structures and properties, through the framework of the defects in diamond, emphasizing the NV centers and their correlation with graphene as the main subject of this thesis. The definition and description of the two charge states of NV centers and their potential use in the quantum technologies are given. Ion implantation, as one of the commonly used techniques nowadays, along with its limiting factors, the spatial resolution and simulation methods is discussed. In the final part of this chapter, the two most important processes in this experiment are explained, the Förster resonance energy transfer and the fluorescence lifetime analysis.

Chapter three focuses mainly on the experiments and the methods used in this work. Beginning with the introduction and description of the three main systems used for the measurements and their function principles. Following the detailed explanation of the whole procedure in steps, from the graphene deposition training through sample preparation including the ion implantation and confocal microscopy measurements that show the results of the implantation procedure and deposition, up to the point where the fluorescence lifetime analysis takes precedence.

In chapter four the results are shown with the discussion of the findings. In the beginning, the photoluminescence spectra of graphene and the implanted region on the sample are presented and fitted. The discussion of the time-resolved fluorescence lifetime measurements follows with the mono- and bi-exponential fits. The parameters and the analysis is accordingly explained. Finally the estimation of the FRET process between the NV centers and graphene is presented.

Chapter 2

Theoretical Background

2.1 Diamond Structure

Diamond is an extraordinary material with an extensive set of applications. It is certainly one of the most prominent materials in terms of its special optical properties. Its unparalleled hardness and thermal conductivity make it a great contender for various applications such as for grinding and polishing tools as well as for heat sinks. Diamond also finds its place in the conventional semiconductor applications like silicon (Si) or gallium arsenide (GaAs). Even though it is perfectly stable under ambient conditions, it is not considered to be a stable allotrope of carbon. All of its exceptional properties have roots in its crystal structure properties.

2.1.1 Diamond crystal structure

Diamond crystal structure consists of covalently bonded carbon atoms where each of the four valence electrons of the sp^3-hybridized carbon engages in bonds with neighbouring atoms at the distance of 1.44 Å. One could expect that these carbon atoms have a filled s orbital and two half-filled p orbitals. However, these orbitals merge and form four new equivalent half-filled sp^3 hybrid orbitals. This rearrangement initially brings about some energy expense, but in the end it allows atoms to make four very strong covalent bonds which completely compensate for the energy expenditure.

The crystal structure of diamond can be thought of as two interpenetrating face-centered cubic (FCC) Bravais lattices with one being displaced by $\frac{1}{4}a(\hat{x}+\hat{y}+\hat{z})$ along the space diagonal of the unit cell (lattice constant 3.57 Å).

From the figure 2.1b it is clear that the coordination number of this structure is 4. Therefore, the space filling is not very efficient. In particular, since each Bravais cell contains eight atoms, the packing fraction in a diamond cubic is:

$$8\frac{4}{3}r^3\pi\left(\frac{8r}{\sqrt{3}}\right)^{-3} = \frac{\sqrt{3}}{16}\pi = 0.340 \tag{2.1}$$

which is just 46 % of the highest packing density possible in crystal structures.

However, diamond lattice is not a Bravais lattice, because the environment of any point is not the same as the environment of its nearest neighbors [13].

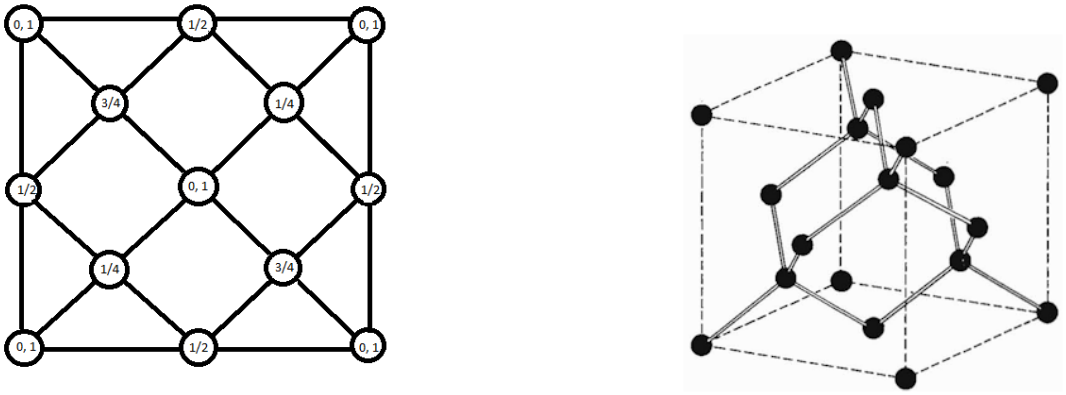

(a) (b)

Figure 2.1: (a) Positions of the atoms in the diamond cubic structure projected onto one of the cube faces, where fractions denote the height of the atom above the base in units of a cube edge[12]. (b) Crystal structure of the diamond cubic showing the two interpenetrating FCC structures, taken from[12].

2.1.2 Electronic structure in the diamond lattice

The electronic band structure or just band structure of a solid is the range of energy levels that electrons may have (allowed bands) or may not have (band gaps or forbidden bands). Band theory is the theoretical model which derives these bands and band gaps by investigating the allowed quantum mechanical wave functions for an electron in a infinite, periodic lattice of atoms. The electrons occupy discrete energy levels of single atoms. When atoms form molecules the atomic orbitals of single atoms overlap and form energy bands. There are several possible methods to examine the band structure of solids, the most common ones being the tight-binding model [14][15], the linear combination of atomic orbitals (LCAO) [14][13] or the empirical pseudo potential method (EPM) [17].

The band structure gives rise to a way to understand the electrical and optical properties of a solid. In order to calculate it (following [14]), one starts from the time independent Schrödinger equation for a single electron

$$\left[-\frac{\hbar}{2m}\nabla^2 + U(\vec{r}) \right] \Psi(\vec{r},\vec{k}) = E(\vec{k})\hat{H}\Psi(\vec{r},\vec{k}). \tag{2.2}$$

Since a lattice is a periodic structure, the potential $U(\vec{r})$ is also periodic and satisfies $U(\vec{r}) = U(\vec{r} + \vec{R}_\mathrm{n})$, where $\vec{r}$ is a lattice vector and $\vec{R}_\mathrm{n}$ is an arbitrary translation vector of the lattice.

In order to determine the band structure of a solid it is sufficient to understand what happens within the first Brillouin zone of the lattice. By definition, Brillouin zone is a uniquely defined primitive cell in reciprocal space. Reciprocal space is a momentum space, also called k-space which is a Fourier transform of the direct lattice. This is where Bloch's theorem comes in handy.

Bloch theorem: An electron in a periodic potential has eigenstates of the form

$$\Psi^\alpha_{\vec{k}}(\vec{r}) = e^{i\vec{k}\cdot\vec{r}} u^\alpha_{\vec{k}}(\vec{r}) \tag{2.3}$$

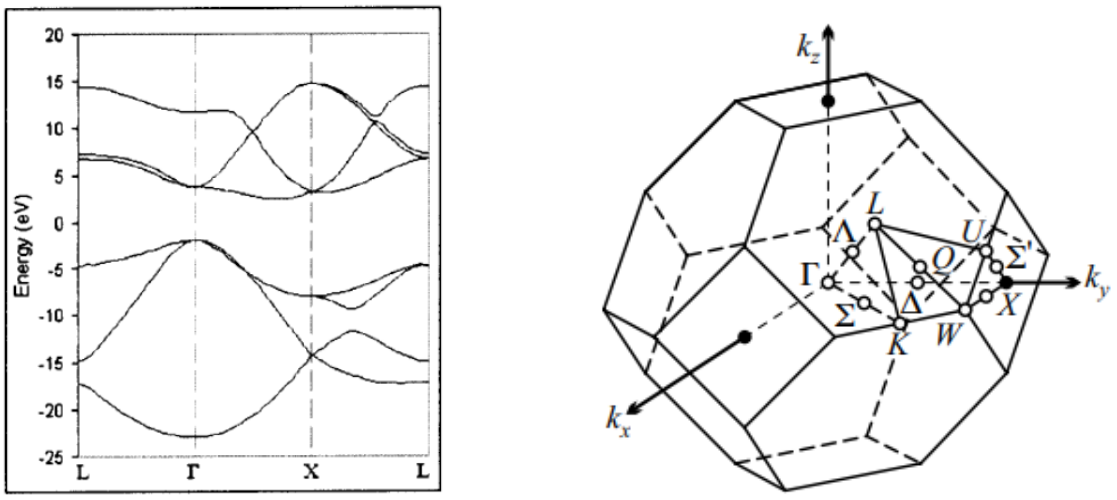

(a) (b)

Figure 2.2: (a) Band structure of diamond starting from point L, through Γ and X. Taken from [21]. (b) First Brillouin zone of the face-centered cubic lattice of the diamond structure with the special points and lines. Taken from [13].

where $u^{\alpha}_{\vec{k}}$ is periodic in the unit cell and $\vec{k}$ (the crystal momentum) can be chosen within the first Brillouin zone.

In a reduced zone scheme there may be many states at each $\vec{k}$ and these are indexed by α. The periodic function u is known as the *Bloch function*, and Ψ is sometimes known as a *modified plane wave*. Because u is periodic, it can be written as

$$u^{\alpha}_{\vec{k}}(\vec{r}) = \sum_{\vec{G}} \widetilde{u}^{\alpha}_{\vec{G},\vec{k}} e^{i\vec{G}\cdot\vec{r}}. \tag{2.4}$$

This form guarantees that $u^{\alpha}_{\vec{k}}(\vec{r}) = u^{\alpha}_{\vec{k}}(\vec{r}+\vec{R})$ for any lattice vector $\vec{R}$. As a matter of fact, the function u is periodic in the unit cell if and only if it can be written as a sum over reciprocal lattice vectors as in equation 2.4. Therefore the complete wavefunction looks like

$$\Psi^{\alpha}_{\vec{k}}(\vec{r}) = \sum_{\vec{G}} \widetilde{u}^{\alpha}_{\vec{G},\vec{k}} e^{i(\vec{G}+\vec{k})\cdot\vec{r}}. \tag{2.5}$$

Hence, an equivalent statement to the Bloch's theorem is that one can write each eigenstate as being made up of a sum of plane-wave states $\vec{k}$ which differ by reciprocal lattice vectors $\vec{G}$. This stems from the Laue condition. As a result the Schrodinger equation is a "block diagonal" in the space of $\vec{k}$, and in any given eigenfunction only plane waves $\vec{k}$ that differ by some $\vec{G}$ can be mixed together [14].

Therefore the view of the solid can be restricted to the first Brillouin zone in reciprocal space. Since each wave vector can be projected into a point within the first Brillouin zone, the special points or the points of interest represent the guidelines, or directions withing the solid in which the band structure is presented. Γ represents the center of the 1st BZ at $\Gamma = (0,0,0)$, X is the center of the square face at $X = (\frac{2\pi}{a})(0,0,1)$ and L is the center of the hexagonal face, as depicted in the figure 2.2b.

2.1.3 Optical properties

The remarkable physical properties of diamond make it a very interesting material for many optical and optoelectronic uses. Completely saturated valence electrons bring about the band gap of 5.49 eV, which makes diamond a very good insulator that is optically transparent in the ultraviolet, visible and also infrared part of the spectrum. That is because the energy of the visible part of the spectrum is in the range of 1.5 eV to 3 eV and the gap is larger than the visible light region. It also possesses a large refractive index of 2.42. This large bandgap makes it a favorable medium for many of the lattice defects to show their optical activity through their electronic and vibrational transitions. In particular the luminescence. Many defects in diamond, showing in the form of vacancy- or interstial-related point defects, can form optical centers, [20]. The impurities in diamond are not equally optically active. Some, like silicon (Si) make only one form of an optical center, while others like for example nitrogen (N) make up a great number of optically active center through the whole optical range of diamond.

Another important optically related feature of diamond is its Debye temperature of about 2000 K, that is the highest known Debye temperature for all solids. This property results in a great excitation of the phonons in the lattice and brings up the electron-phonon coupling in optically active defects at high temperatures.

Raman spectroscopy is a very useful technique used to analyze many different types of structures including solids, liquids or gasses. Raman spectroscopy is essentially a non-destructive technique that involves visible light and observation of the scattered light off of chemical bonds in the material. When light is shown on the material, most of the scattered light is in the close range of the incident light wavelength, which is called *Rayleigh scattering*. However, a small portion of light (on the order of 10^{-7} %) gets scattered at different wavelengths and this is called *Raman scattering*. This happens due to the chemical structure of the material which is the subject to analysis. A Raman spectrum is a collection of peaks at different wavelengths with certain intensities and it is considered to be a chemical fingerprint of a material. Each peak corresponds to a specific molecular bond vibration.

According to [20], diamond shows the Raman scattering cross-section of $r_{sp^3} = 9 \times 10^{-7}$ $cm^{-1}sr^{-1}$. Because of the long wavelength of light in comparison with the Brillouin zone dimensions, only the zone center phonons (the 1332 cm^{-1}) are normally observed in the first-order Raman spectrum of diamond. There is also a very characteristic peak for diamond, at a wavenumber 2670 cm^{-1}, the second-order Raman peak, that is the consequence of the density of states peak at 1335 cm^{-1}. It is interesting that the second-order Raman peak is much more strongly excited from within the UV range.

2.1.4 Classification

Natural diamonds are classified according to their optical properties and the number of nitrogen impurities contained. The majority of natural diamonds are Type I, with an absorption edge of about 330 nm (more than 98 % of natural diamonds) with the concentration of nitrogen impurities of 100 ppm to 3000 ppm, while the smaller group Type II has an absorption edge of about 220 nm and has a very low nitrogen concentration, typically less then 5 ppm.

Type I:

1. Type Ia - contains aggregated nitrogen;
    - Type IaA - Nitrogen atoms are present in the form of pairs or small groups (A aggregates[1].);
    - Type IaB - Nitrogen atoms are present as isolated atoms (B aggregates).
2. Type Ib - contains single substitutional nitrogen.

Type II:

1. Type IIa - Mostly pure, having no significant impurities;
2. Type IIb - Boron atoms are the major impurity and they make a p-type semiconductor.

Most of the high pressure high temperature (HPHT) grown diamonds fall under the type Ib group and most chemical vapour deposition (CVD) grown diamonds fall under type IIa, due to their different nitrogen levels, [23].

However this classification is oversimplified for many of the polycrystalline and single crystal grades, developed with specific properties that this system[19] does not distinguish between.

2.2 Defects in Diamond

Defects or impurities are imperfections in the periodic structure of solids. They largely affect mechanical and electrical properties of solids. There are many different types of defects that occur: point defects, line defects, planar defects and bulk defects [22].

Point defects are all defects that consist of one or a few atoms extra or missing, at or around a single lattice point. They do not extend in space in any dimension. Most important ones are:

- *Vacancies* - vacant lattice sites that are normally occupied in a perfect crystal. If a neighboring atom moves towards the vacancy as if to fill it, the vacancy moves in the opposite direction and takes the place of the moving atom. This does not affect the stability of the surrounding structure.
- *Interstitials* - an atom occupies a site which is not occupied in a perfect crystal. This generally happens in high energy arrangements, but also sometimes with a smaller atom and lower energy, i.e. hydrogen in palladium.
- *Frenkel defect* - a combination of a vacancy and an interstitial which forms as a pair (also called a Frenkel pair), when an atom moves to an interstitial position and creates a vacancy.

[1]The aggregates A, B and B' were first discovered by Sutherland in 1954. See [20]

Line defects or **dislocations** are lines within a crystal structure along which whole rows of atoms are arranged anomalously. They appear as edge and screw dislocations or in combinations of both types. The line along which the dislocation happens is called the *disclocation line* (See [20][23]).

Lately, there has been s a large interest in diamond in material science. This comes from the fact that the defects in diamond often have very low electron-phonon coupling because of the low density of phonon states, as well as because the colour centers in diamond are very stable generally with long coherence times (up to ∼2 ms) even under room temperature conditions, [24], which makes for remarkable optically active solid-state systems. There are more than five hundred luminescent defects discovered to be present in diamond out of which only less then ten have been identified as bright, stable, single-photon emitters. In this work, nitrogen related defects, particularly nitrogen-vacancy centers are of most importance.

2.2.1 Nitrogen-vacancy centers

The nitrogen-vacancy center (mostly referred to as NV center shorter) is one of the most common and studied defects in diamond. It is a point defect consisting of a nitrogen atom paired with a vacancy following along the [111] crystalline direction. It follows a C_{3v} symmetry and can be formed as a product of the growth of CVD diamonds, radiation damage or ion implantation in both bulk diamonds and nanodiamonds[26]. So far it has been found to have two charge states, neutral NV^0 and negative NV^- charge state. There are some speculations and theories about the positive NV^+ charge state, but to date there has not been a clear discovery of such.

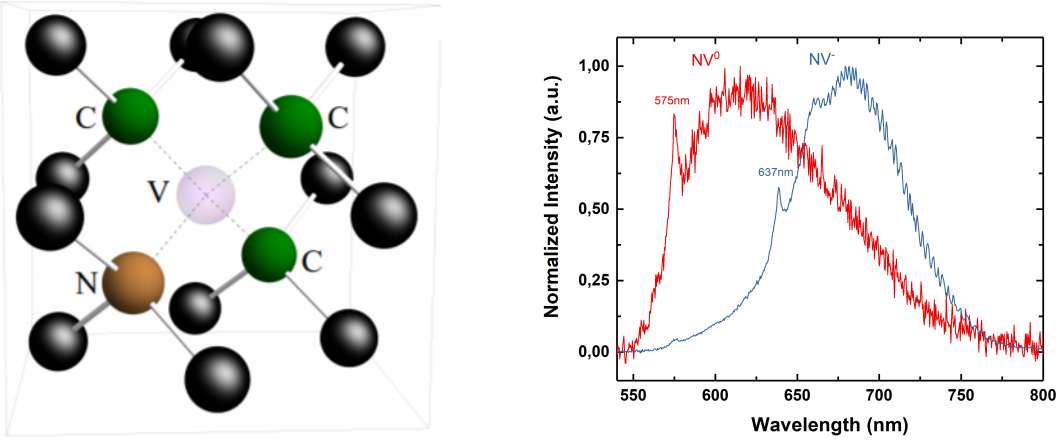

(a) (b)

Figure 2.3: (a) The atomic structure of the NV center in the diamond crystal lattice[26], where the vacancy is transparent, the nearest neighboring carbon atoms are shown in green and the nitrogen substitutional atom shown in brown. (b) The characteristic spectra of the NV^0 and NV^- with their zero-phonon lines (ZPL) at 575 nm and 637 nm respectively.

NV^0 center is often present in the nitrogen rich type Ib diamonds it is formed according to $N + V \rightarrow NV^0$. It has 5 electrons, 3 from neighboring carbon atoms and 2 from the intrinsic nitrogen atom[25, 26]. It is an $S = 3/2$ spin system. The

photoluminescence of the center exhibits a zero-phonon line at 2.156 eV (575 nm) with a characteristic broad phonon sideband extending from 580 nm to 650 nm. Its electronic structure (Figure 2.4a) has been studied through electron paramagnetic resonance (EPR). The optical transition happens between the doublet ^2E ground and the $^2A_2$ excited states. Further, there has been a discovery of the electron spin resonance signal associated with a quartet $^4A_2$ intermediate state.

NV$^-$ center is formed when in the vicinity of the NV^0 center there is a substitutional nitrogen atom which donates an extra electron and follows $NV^0 + N \rightleftharpoons NV^- + N^+$. Therefore, it has 6 unpaired electrons, same as NV^0 with an additional electron trapped at the defect site that is the origin of its negative charge state. It is the only diamond color centre that has shown coherent optical effect such as electromagnetically induced transparency and coherent population trapping. It exhibits a relatively strong overall electronic dipole moment of about 2×10^{29}Cm, although only 4 % of its emission is concentrated in the ZPL with a Debye-Waller factor of 0.04 [25].There is also an additional ZPL in the infrared range at 1.190 eV (1042 nm) associated with NV$^-$ center [26]. Since, it has an even number of unpaired electrons and a C_{3v} symmetry, it is a $S = 1$ spin system and from group theory it follows that the many electron configuration forms spin triplet states ($^3A_2$ and ^3E), and spin singlet states (^1A and ^1E), see figure 2.4.

Under optical illumination NV^0 and NV$^-$ centers exhibit an excited state lifetime of ~ 20 ns(according to my supervisor) and 12.9 ± 0.1 ns [25], respectively, in bulk diamond.

From Figure 2.3b it is clear that the spectra of both charge states of the NV centers significantly overlap. In many instances both NV^0 and NV$^-$ centres can be found within the same defect center.

The sharp ZPLs and well-defined vibronic bands of the two NV charge states stipulate the occurrence of the optical transition between discrete energy levels that are deep within the diamond band gap. The NV centers are thus known as the deep-level defects in diamond.

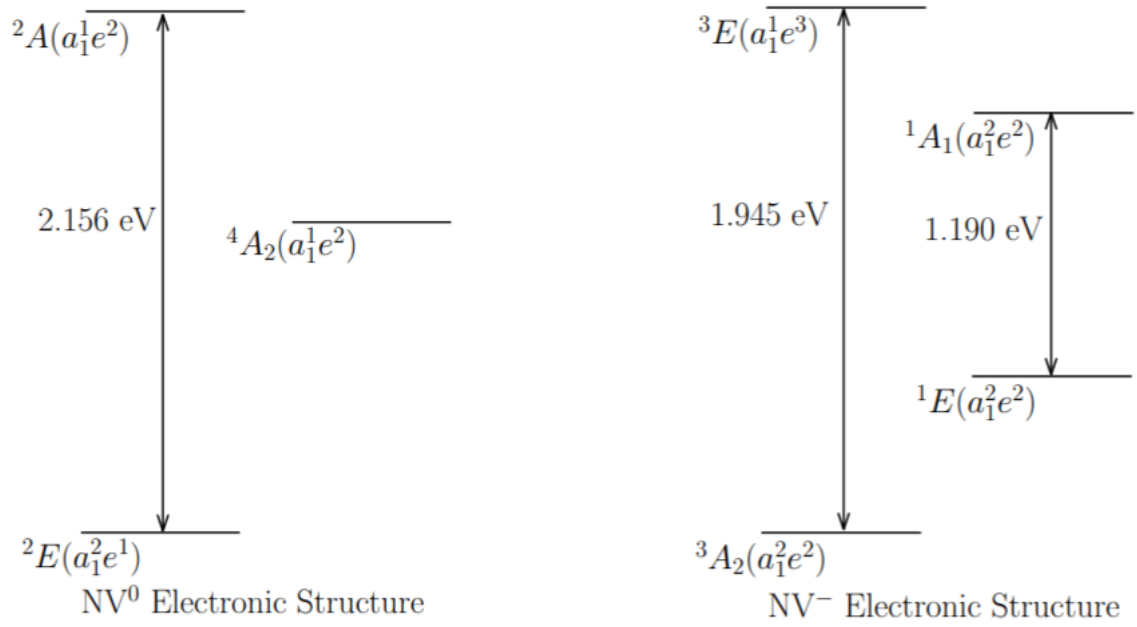

(a) (b)

Figure 2.4: Electronic structures of the two charge states of NV centers[26]. Indicated with arrows are the energies of the known ZPL transitions between the electronic levels.

2.3 Ion Implantation

Ion Implantation is a technique used to modify the physical, chemical and optical properties of a material by introducing foreign atoms (impurities) into the lattice. It is mostly used in semiconductor fabrication and material science research.

Dopant atoms are ionized, accelerated and directed towards a target. Such ions enter the lattice, collide with its atoms losing energy and eventually come to a stop at some depth in the solid. The average penetration depth depends on the dopant, the target material and the acceleration energy used, [9]. Energies of the ions typically used range from a few hundreds of eV to a few MeV which results in average penetration depth from less than 10 nm to approximately 10 µm. Doses typically used range from 10^{11} atoms/cm^2 to 10^{18} atoms/cm^2.

2.3.1 Ion stopping

As ions travel through the target material, they lose energy. But, since the energies of ions are typically much higher than the lattice binding energies, the ion scattering can be simulated based on elastic collisions between two atoms without regard for the relatively weak lattice forces. The other componenet of scattering comes from the inelastic collisions with electrons in the material, [9, 10]. Therefore the full stopping power S of the target defined as the energy loss per unit path length of the ion can be written as:

$$S = \left(\frac{dE}{dx}\right)_{\text{nuclear}} + \left(\frac{dE}{dx}\right)_{\text{electronic}}. \tag{2.6}$$

Nuclear stopping can be described by classical kinematics since it is caused by a collision between two atoms. When the atoms are considered to be bare nuclei, the Coulomb potential between them is:

$$V_c(r) = \frac{q^2 Z_1 Z_2}{4\pi\epsilon_0 r} \tag{2.7}$$

where Z_1, Z_2 are the atomic numbers of the two nuclei (implanted and target atoms respectively), ϵ_0 is the permittivity and q is the electronic charge. Electrons in reality screen the nuclear charge so the screening function $f_s(r)$ must be included so that:

$$V(r) = V_c(r) f_s(r). \tag{2.8}$$

Working in the center-of-mass frame, the solution to the equations of motion of such a system yields the scattering angle for incident ion trajectory according to the equation:

$$T = \frac{4M_1M_2}{(M_1+M_2)^2} E sin^2\left(\frac{\theta}{2}\right) \tag{2.9}$$

where T is the energy lost by the ion, E is the initial energy of the ion, Θ the scattering angle and M_1, M_2 are the atomic mass numbers of the ion and the target atoms respectively. If the maximum energy transfer in a collision is $T_{\max}$ and there are N target atoms per unit volume then

$$S_n = \left(\frac{dE}{dx}\right)_{\text{nuclear}} = N\int_0^{T_{\max}} T d\sigma \tag{2.10}$$

where $d\sigma$ is the differential cross section. Nuclear stopping is elastic and thus the energy lost by the ion is transferred to the target atom which gets ejected from its lattice site creating further damage and a defect site.

Electronic stopping, on the other hand, is inelastic and while the theoretical model is quite complex, for low energies, the stopping can be understood as the viscous drag force proportional to the ion velocity and he energy loss is dissipated through the electron cloud into thermal vibrations of the target.

2.3.2 Range distributions

Accelerated ions traverse a random path while travelling through the target decreasing their energy with nuclear and electronic stopping. Ion paths can be predicted using statistical approximations as long as the doses are higher than $10^{12} ions/cm^2$. The range R is constructed taking into consideration both lateral and vertical motion, [10]. The projected range R_p can be approximated as a Gaussian distribution with standard deviations σ_p for the projected range and $\sigma_\perp$ for lateral motion. At distances far enough from the mask edges the lateral motion can be neglected which leads to a concentration at depth x:

$$n(x) = n_0^{-\frac{(x-R_p)^2}{2\sigma_p^2}} \tag{2.11}$$

where n_0 is the peak concentration. Then:

$$n_0 = \frac{\phi}{\sigma_p\sqrt{2\pi}} \simeq \frac{0.4\phi}{\sigma_p} \tag{2.12}$$

with ϕ being the total implantation dose.

2.3.3 Limiting factors and the spatial resolution

The Spatial resolution is a measure of the precision of the final position of the ions within the target, [9]. The most important is the lateral resolution (the implantation depth) which is a direct consequence of the kinetic energy of the ion as well as its mass, and is limited by:

- *Ion Straggle* - the spread of the ions along the beam. In other words, it is a an intrinsic physical limitation of the spatial resolution depending on many factors such as: the particle accelerator itself, ions used, target material, temperature, crystal orientation, etc. It can be understood as the scattering of the ions impinging on the target which creates a broadening in the beam creating an uncertainty in the final position of the ions implanted. It is minimal at low energies on the order of 10 keV.

- *Ion Channeling* - certain directions in the crystalline material serve as paths through which ions can pass without much scattering which leads to much longer penetration depths or sometimes even ions passing thorugh the whole target and exiting on the other side. Channeling is characterized by a critical angle Ψ_1 which is defined as the maximum angle between the ion and the channel for a glancing collision to occur:

  $$\Psi_1 = 9.73\left(\frac{Z_1 Z_2}{Ed}\right)^{1/2} \tag{2.13}$$

  ignoring the thermal vibrations, where E is the ion energy and d is the atomic spacing, [10]. It shows that the channeling process is more likely to occur for heavier ions and lower energy. That is why the wafers are usually tilted by an angle of 7° to avoid the major planes within the crystal.

2.3.4 Damage

As ions traverse the target material they undergo a series of collisions transferring energy to the target atoms which creates cascades. As the energy gets dissipated between the atoms during the collisions, the cascade stops leaving the target in a highly disordered state. If the target is at a high enough temperature it is possible that *self-annealing* will occur repairing the lattice partially. However, it is a standard procedure to use the process of *annealing* after the implantation is done.

Annealing

Due to severerity of the damage done on the target material, the electrical properties of the material are strongly changed by the deep-level electron and hole traps that increase the resistivity substantially, [10]. The annealing or the recrystalization

process is done in order to repair the damage and put the doped atoms on substitutional sites. In the context of this work, this process allows the vacancies to become mobile and travel to the implanted nitrogen atoms which is how NV centers are formed. It is done at very high temperatures, typically on the order of 800 °C for several hours in high temperature ovens, often made from graphite.

2.3.5 SRIM

Stop and Range of Ions in Matter (SRIM) is a program used to numerically simulate the process of ion implantation, i.e. the penetration depth and range of ions in the target material. It employs the Monte Carlo algorithm to calculate the interaction of accelerated ions with the target. It uses an analytical formula to simulate the collisions between atoms as well as a free-flight-path method between collisions in order to evaluate only the significant collisions. It is a very useful tool for making predictions based on the ion energies that gives the range and the implantation depth and the dose which allows to estimate the concentration of vacancies made in this region.

2.4 Graphene

Carbon, as the fourth most abundant element on earth shows a wide range of bonding possibilities makes it the most important element for research in a variety of disciplines. It allows the formation of large stable frameworks of interconnecting bonds with different hybridization which makes up an uncountable amount of compounds with different dimensions [28]. Recently, there has been an addition to this large family of carbon allotropes, the first graphene was experimentally isolated back in 2004, and has been a subject of extensive research since. It can be considered as the compound which when subjected to different folding techniques (see Figure 2.5) can reproduce all of the other allotropes of carbon. In that sense it is understood as a parental compound for them (i.e. the wrapping of graphene with a curvature intervening five membered rings results in creation of a fullerene, while the rolling of graphene produces carbon nanotubes, etc.). It is potentially a significantly important material with applications in nanotechnology, 'beyond-silicon' electronics, solid state realization of high-energy physics and is expected to be also important as a membrane that could bring up a revolution in soft-matter and two-dimensional physics [27].

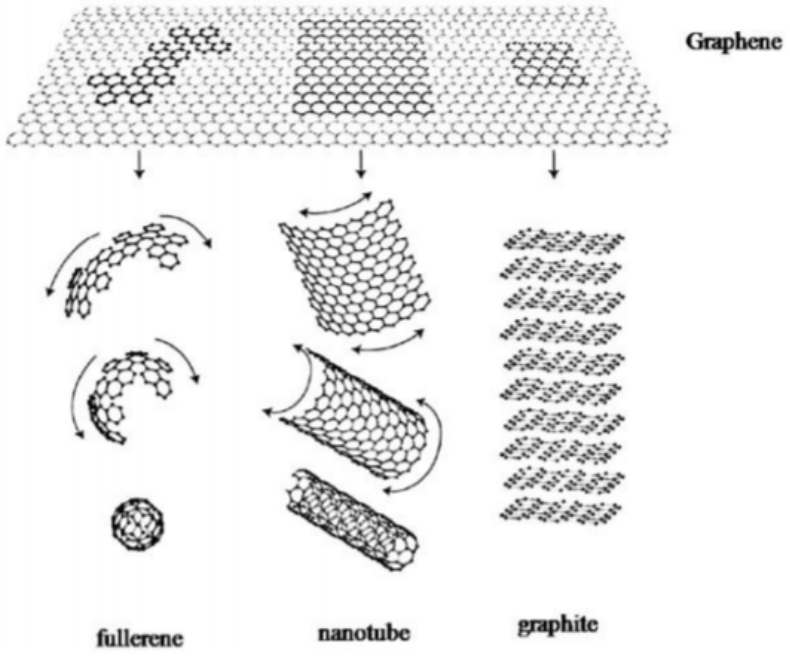

Figure 2.5: Graphene as the parental compound for allotropes of carbon [28].

Graphene has been found to possess a variety of extraordinary properties. It exhibits high electrical and thermal conductivities, with unprecedented elasticity and flexibility as well as hardness. In strength it is similar to diamond (approximately two hundred times stronger than steel). It shows a low electricity consumption in comparison to other compounds and it can even have an antibacterial effect or generate electricity just from exposure to sunlight.

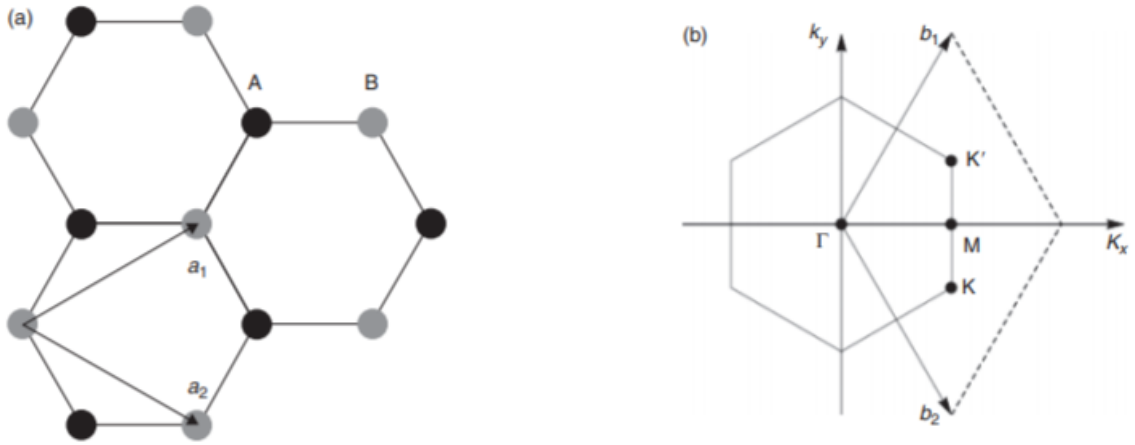

(a) (b)

Figure 2.6: Lattice vectors of the graphene honeycomb structures are shown in (a) along with the two sublattices **A** in black and **B** in light grey, and in (b) one can see the Brillouin Zone with reciprocal lattice vectors and some special high-symmetry points [27].

2.4.1 Graphene structure

Graphene is comprised of carbon atoms. Carbon atom is the sixth element in the Periodic Table with two stable isotopes ^{12}C with a nuclear spin $I = 0$ and magnetic moment $\mu_n = 0$, and ^{13}C with $I = 1/2$ and $\mu_n = 0.7024\mu_N$ (where μ_N is the nuclear magneton) [27]. It has six electrons out of which two form a closed $1s^2$ shell and four fill 2s and 2p states, with ground state atomic configuration $2s^2\ 2p^2$, total spin $S = 1$, total orbital moment $L = 1$ and total angular moment $J = 0$.

Graphene has a honeycomb crystal lattice (see Figure 2.6a) with a triangular Bravais lattice and lattice vectors:

$$\vec{a}_1 = \tfrac{a}{2}(3, \sqrt{3}), \quad \vec{a}_2 = \tfrac{a}{2}(3, -\sqrt{3}), \tag{2.14}$$

where $a \approx$1.42 Å is the nearest neighbor distance. It contains two atoms per unit cell which belong to two sublattices **A** and **B**, such that each atom in sublattice **A** is surrounded by three atoms from sublattice **B** and vice versa. The reciprocal lattice is triangular as well (see Figure 2.6b), with lattice vectors:

$$\vec{b}_1 = \tfrac{2\pi}{3a}(1, \sqrt{3}), \quad \vec{b}_2 = \tfrac{2\pi}{3a}(1, -\sqrt{3}). \tag{2.15}$$

Electronic structure

To obtain the electronic structure of graphene and consecutively graphite, one starts with the sp^2 hybridized states, σ states that form occupied and empty bands with a huge gap and π states that form a single band with a conical self-crossing point in **K** and due to symmetry in **K'** as well (see Figure 2.6b). This conical point is the origin of the extraordinary electronic properties of graphene.

Starting from the tight-binding model in the nearest-neighbor approximation for the π states only, with the hopping term t (following [27]). In the basis, there are two π states for each of the atoms in sublattices **A** and **B**. There are no hopping

processes within the sublattices, but rather the hopping takes place only between them, according to the nearest-neighbor approximation. Therefore the Hamiltonian for the tight-binding model becomes a 2×2 matrix of the form

$$\hat{\mathbf{H}}(\vec{k}) = \begin{pmatrix} 0 & tS(\vec{k}) \\ tS^*(\vec{k}) & 0 \end{pmatrix} \tag{2.16}$$

where $\vec{k}$ is the wave vector and

$$S(\vec{k}) = \sum_{\vec{\delta}} e^{i\vec{k}\vec{\delta}} = 2\exp\left(\frac{ik_x a}{2}\right) cos\left(\frac{k_y a\sqrt{3}}{2}\right) + \exp(-ik_x a). \tag{2.17}$$

The energy is then,

$$\mathbf{E}(\vec{k}) = \pm t|S(\vec{k})| = \pm t\sqrt{3} + f(\vec{k}), \tag{2.18}$$

where

$$f(\vec{k}) = 2cos(\sqrt{3}k_y a) + 4cos\left(\frac{\sqrt{3}}{2}k_y a\right) cos\left(\frac{3}{2}k_x a\right). \tag{2.19}$$

From $S(\vec{\mathbf{K}}) = S(\vec{\mathbf{K}}\text{'}) = 0$ it is clear there is a band crossing. After expanding the Hamiltonian around these points one reaches the effective Hamiltonians near the points **K** and **K'**

$$\hat{\mathbf{H}}_{\mathbf{K},\mathbf{K}'}(\vec{q}) = h\nu \begin{pmatrix} 0 & q_x \mp iq_y \\ q_x \pm iq_y & 0 \end{pmatrix} \tag{2.20}$$

where

$$\nu = \frac{3a|t|}{2} \tag{2.21}$$

represents the electron velocity at the conical points. Taking into account the next-nearest-neighbour hopping t', it follows for the energy

$$\mathbf{E}(\vec{k}) = \pm t|S(\vec{k})| + t'f(\vec{k}) = \pm t\sqrt{3} + f(\vec{k}) + t'f(\vec{k}). \tag{2.22}$$

Even though the second term breaks the electron-hole symmetry, shifting the conical point from $\mathbf{E} = 0$ to $\mathbf{E} = -3t'$, it does not change the behaviour of the Hamiltonian near the conical points. Furthermore, it has been proven that this behaviour is symmetry- and topologically-protected (for more see [27]).

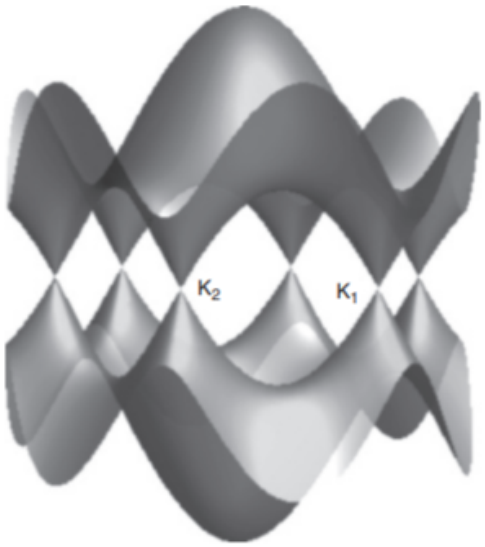

Figure 2.7: Electron energy spectrum of graphene in the nearest-neighbour approximation with the conical points marked as K_1 and K_2 [27].

2.4.2 Raman spectrum of graphene

The Stokes phonon energy shift caused by the laser excitation creates two main peaks in the Raman spectrum of graphene. The G peak ($1580\,\mathrm{cm}^{-1}$), a primary in-plane vibrational mode, and a 2D peak ($2690\,\mathrm{cm}^{-1}$), a second-order overtone of a different in plane vibration and a D peak ($1350\,\mathrm{cm}^{-1}$).

Due to the interactions between layers of graphene, namely the additional forces created by the layers, as the number of layers increases, the spectrum changes. there is a splitting of the 2D peak into an increasing number of modes that can interact, and the G peak experiences a small red shift [29]. Hence, for the AB-stacked graphene, the number of layers can be calculated from the position and the shape of the 2D and G peaks and the ratio of peak intensities, I_{2D}/I_G.

The first-order D peak is not normally visible in pristine graphene because in order for it to appear, a charge carrier must be excited and scattered inelastically by a phonon, then successively elastically scattered by a zone boundary or a defect to result in recombination [29]. The 2D peak is always allowed because the second scattering is also an inelastic scattering from a second phonon. Characteristic spectra of a single-layer graphene is shown in Figure 2.8.

A very important property of graphene to be determined is the level of disorder within the structure and it can be described by the ratio of intensities of the D and G peaks, I_D/I_G. It has been shown[29], that I_D/I_G exhibits two different behaviours for the two different regimes. For the regime of the *low* defect density it increases as the defect density increases and creates more elastic scattering, while for the *high* defect density regime it begins to decrease as the defect density increases resulting in a more amorphous carbon. This shows as an attenuation of all the Raman peaks. These two regimes are known as the *nanocrystalline graphite* and the *mainly* sp^2 *amorphous carbon* phases, respectively.

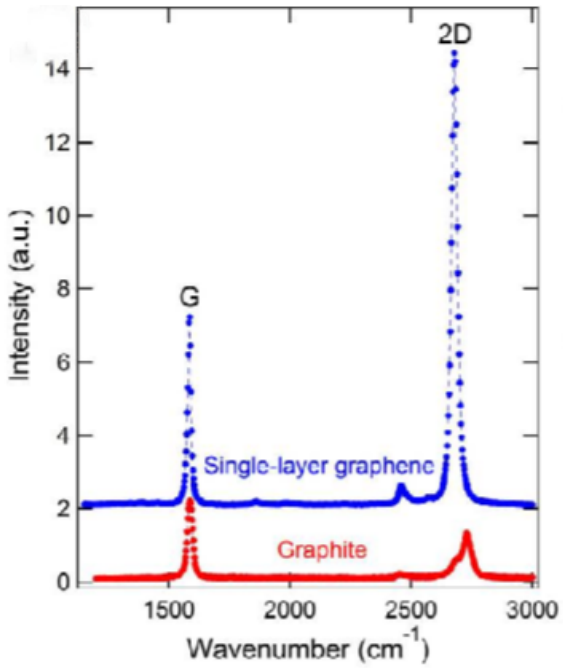

Figure 2.8: From [29], typical Raman spectrum for a single-layer graphene and bulk graphite using 532 nm excitation laser. Graphene can be identified by the position and the shape of its G peak at 1580 cm^{-1} and the 2D peak at 2690 cm^{-1}.

2.5 FRET - Förster Resonance Energy Transfer

Förster resonance energy transfer is the process that describes the energy transfer from a fluorescent donor molecule in the electrically excited state to the acceptor molecule in ground state through nonradiative dipole-dipole coupling [30, 32]. It is analogous to near-field communication, since the wavelength of the emitted light is much larger than the radius of interaction. What essentially happens is that the donor emits a *virtual* photon that gets immediately absorbed by the acceptor. FRET is known as radiationless process because virtual photons are undetectable thus they contradict the conservation of energy and momentum. Its only limitation is that the radius of interaction must be smaller than 10nm.

2.5.1 Theoretical basis

The dipole-dipole interaction and the efficiency of the energy transfer are strongly dependent on the distance. FRET offers an alternative way for the donor to relax back to the ground state, from the radiative and non-radiative processes. More detailed analysis and explanation of FRET can be found in [33]. The efficiency of FRET is defined as the quantum yield of the energy transfer, the fraction of the energy transfer per donor excitation:

$$E_{\mathrm{FRET}} = \frac{k_{\mathrm{FRET}}}{k_f + k_{\mathrm{FRET}} + \sum k_i} \tag{2.23}$$

where k_{FRET} is the rate constant for FRET, k_f is the rate of the radiative relaxation, or in other words the fluorescence and k_i are the rates of the non-radiative relaxation, like internal or external conversion [30, 31].

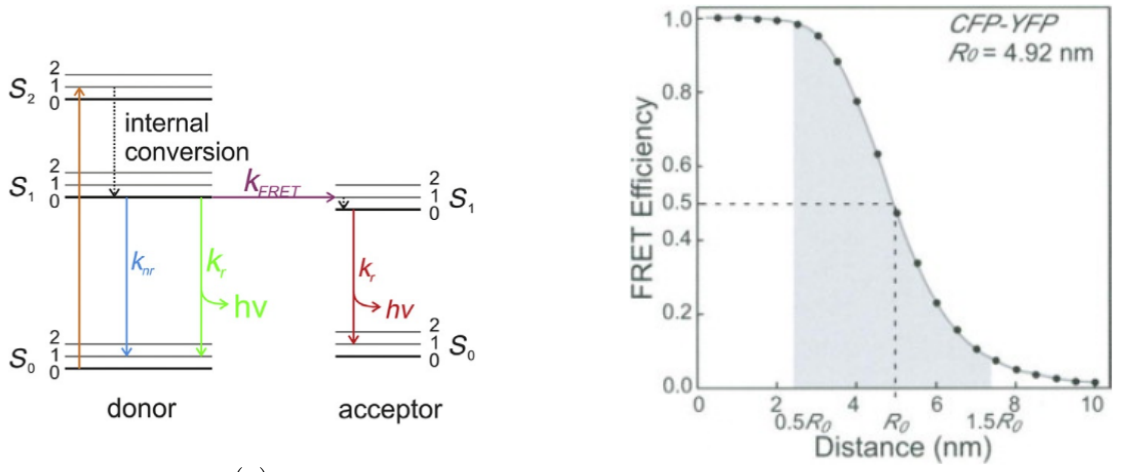

(a) (b)

Figure 2.9: (a) From [30], Jablonski diagram of a FRET process. Excitation of the donor from the ground state S_0 to either the first excited state S_1 or a higher excited state, i.e. S_2 shown in *orange*, is followed by a return to the S_1 by internal conversion. From the S_1 state the donor can return to the ground state by non-radiative transfer in *blue* or radiative processes (donor fluorescence) in *green* or by energy transfer to the acceptor in *purple*. For the acceptor one can see only the radiative transfer (acceptor fluorescence) in *red*. The rate constants of relaxation are k_r, k_nr and k_FRET by radiative, non-radiative processes and FRET, respectively. (b) From [34], graph of the efficiency dependence on the distance between the donor and the acceptor, with R_0 as the Förster radius.

The rate constant k_FRET is proportional to the inverse sixth power of the distance between the donor and the acceptor, r:

$$k_\mathrm{FRET} = \frac{1}{\tau_\mathrm{D}} \left(\frac{R_0}{r} \right)^6 . \tag{2.24}$$

Here, τ_D is the lifetime of the excited state of the donor, and is defined as $\tau_\mathrm{D} = \frac{1}{k_\mathrm{f} + \sum k_\mathrm{i}}$ and R_0 represents the characteristic distance or the Förster radius at which the efficiency is 50 %. From here, taking into account Equation 2.23 and Equation 2.24 we can conclude for the FRET efficiency:

$$E_\mathrm{FRET} = \frac{R_0^6}{r^6 + R_0^6} = \frac{1}{1 + (\frac{r}{R_0})^6} \tag{2.25}$$

The Förster radius, R_0 corresponds to the spectral properties of the donor and the acceptor as a pair, especially on the quantum yield of the donor, ϕ_D, the overlap integral J that measures the overlap of the donor emission spectrum and the acceptor absorption spectrum, as well as on the orientation factor κ^2 that describes the relative orientation of the transition dipoles of donor and acceptor:

$$R_0^6 = \frac{9 ln 10 \phi_\mathrm{D} \kappa^2}{128 \pi^5 N_\mathrm{A} n^4} J \tag{2.26}$$

where N_A is Avogadro's number, n is the refractive index of the medium. The overlap integral J (see Figure 2.10) can be calculated from the normalized emission

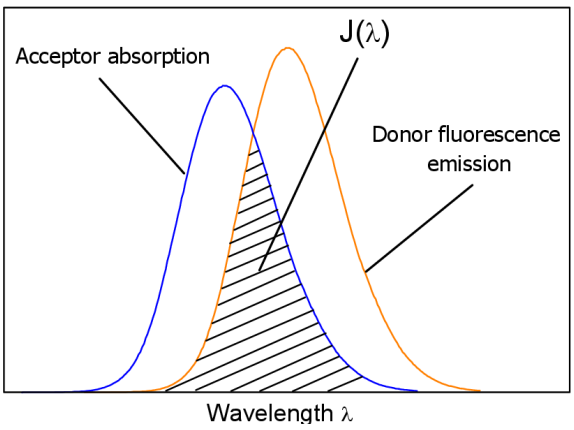

Figure 2.10: From [35], Schematic representation of the spectral overlap integral $J(\lambda)$ for a FRET process.

of the donor F_{D} and the extinction coefficient of the acceptor ϵ_{A} in the region of the spectral overlap:

$$J = \int_{\lambda_{\min}}^{\lambda_{\max}} F_{\mathrm{D}}(\lambda)\epsilon_{\mathrm{A}}(\lambda)\lambda^4 d\lambda. \tag{2.27}$$

Furthermore, the efficiency can also be related to the fluorescence lifetime of the donor molecule in the presence and in the absence of the acceptor, to be precise to the ratio of those lifetimes, in the following way:

$$E_{\mathrm{FRET}} = 1 - \frac{\tau_{\mathrm{D}'}}{\tau_{\mathrm{D}}} \tag{2.28}$$

where $\tau_{\mathrm{D}'}$ and τ_{D} are the fluorescence lifetime of the donor in the presence and the absence of the acceptor, respectively, or as

$$E_{\mathrm{FRET}} = 1 - \frac{F'_{\mathrm{D}}}{F_{\mathrm{D}}} \tag{2.29}$$

where F'_{D} and F_{D} are the donor fluorescence intensities with and without the presence of the acceptor [36].

Chapter 3

Methods and Implementation

In this section the detailed process of the sample preparation for the fluorescence measurements is discussed. Beginning with the cleaning procedure, through ion implantation and confocal measurements, the steps of preparation are discussed chronologically. Additionally, the explanation of the setup for fluorescence lifetime measurements is given.

3.1 Sample Preparation

3.1.1 Cleaning of the substrates

All of the substrates used in this work have been cleaned by the same process. The substrates were first put in ethanol and then submitted to ultrasonic cleaning for several minutes, usually 3-5 minutes, depending on the amount of dirt seen under the optical microscope (Olympus BX51 with an integrated camera, Camera View II Soft Imaging System, see Figure 3.2a). Then, the substrates are taken out and blow dried. For additional cleaning when needed, lens tissues (ThorLabs MC-5) doused in ethanol were used and it proved to be the most effective way of cleaning the surface.

(a) (b) (c)

Figure 3.1: Images of the: (a) Branson Sonifier 250 with the possibility of continuous sonication as well as periodic bursts with controllable power and frequency. (b) Blow dry used for all the sample drying and the evaporation of ethanol. (c) Eppendorf in the range of 1 µL to 100 µL used for solution depositions.

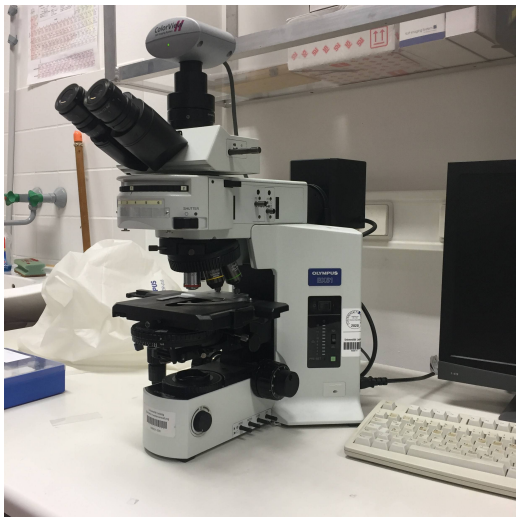

(a)

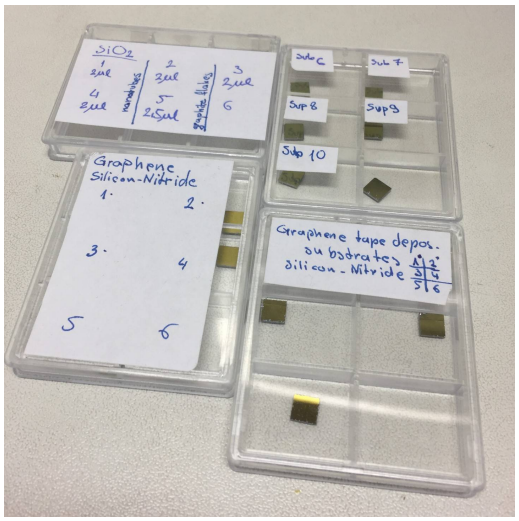

(b)

Figure 3.2: (a) Image of the optical microscope used in this work. (b) Image of all the training substrates used (both Si_3N_4 and SiO_2).

3.1.2 Deposition training

In the very beginning of this work, two methods of deposition were experimented with. Silicon nitride (Si_3N_4), silicon dioxide (SiO_2) of the size 5 mm×5 mm (see Figure 3.2b) and diamond of the size 2 mm×2 mm were used as substrates. Silicon nitride and silicon dioxide, used as training samples, provide more contrast on the optical microscope which made it easier to see graphene and boron nitride layers on the surface and get used to what they look like under different conditions. Since diamond is transparent, it is harder to find monolayers and few-layered flakes on it than on Si_3N_4 and SiO_2. For comparison see Figure 3.5 and Figure 3.13b.

The idea was to try and do the following depositions and then measure the fluorescence from all of them:

1. *Graphene solution deposition* - Pristine Graphene Flakes PGF-1 Monolayer 50ml, Flakes in Ethyl Alcohol made by Graphene Supermarket® with a concentration of 1 mg/L, carbon content 99.99%, ultrapure with no surfactants and no exidation, an average flake thickness of 0.35 nm (1 monolayer) and an average particle (lateral) size of 550 nm was used;

2. *Boron nitride (BN) solution deposition* - Boron Nitride Micropowder 100 g, BN/CAS, 10043-11-5, with a molecular weight of 24.82 g/mol, purity 98%, average particle size of 4 µm and a specific surface area of 7.5 also made by Graphene Supermarket® was used;

3. *Graphene tape deposition* - fine graphite HOPG ZYA SN35587 with 0.4° maximum angle of the layers was used.

Using the solution of graphene proved to be hard and unforgiving as in every attempt the substrates would have dirt and ethanol evaporation marks as well as chunks of graphite or folded sheets of multilayered graphene left on the surfaces, with sporadic very small in size (≤1 µm) and hard to spot graphene flakes (see

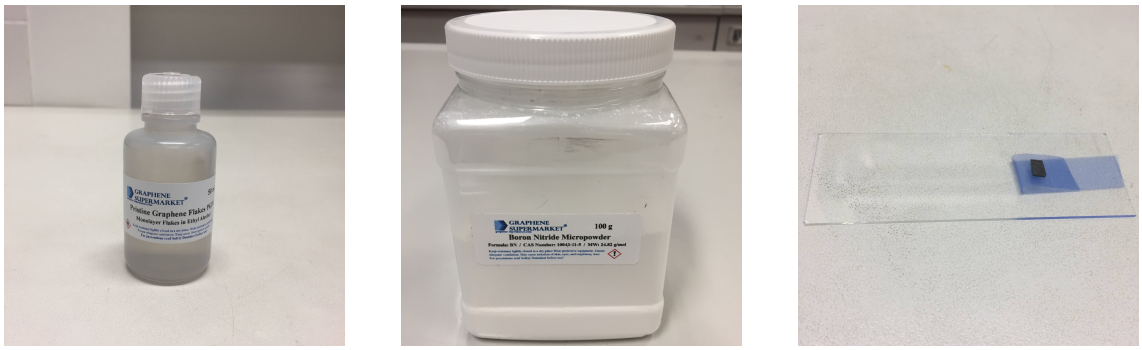

(a) (b) (c)

Figure 3.3: Images of the: (a) graphene solution, (b) boron nitride solution and (c) graphite on tape, used for this work.

Figure 3.4). The hard part was to remove the dirt without removing the flakes with it as well. Different concentrations were also attempted (2x, 3x, 4x and 5x the initial concentration) but none of them turned out to be useful, giving better results. As for the BN solution, it was calculated that the needed concentration of the powder in isopropanol was about 2 mg/L but it showed the same behavior as graphene solution. The droplet size for Si_3N_4 and SiO_2 was determined to be best at 7 µL, and for diamond it was 4 µL, based on the surface area of the substrates. The droplets were put on the surface of the substrates using an eppendorf (see Figure 3.1c). Consequently, evaporation with and without a heater was attempted as well, without any changes. In the end, it was clear that the best results using a solution were made with a blow dry, but even then they were altogether unsatisfactory (see Figure 3.4).

Eventually, it was concluded that the tape deposition was by far the easiest and most useful method of graphene deposition to work with under the currently accessible conditions. Although, it is tricky to use tape deposition, because it requires some practice and experience as to the amount of exerted pressure on the surface as well as the time which the graphene stuck to the surface of the material can withstand the ultrasonic for, in order to achieve few-layered flakes and monolayers for good measurements. It proved to be the most consistent way of creating the desired thickness and positioning of the flakes.

The positioning of the flakes is very important for successful measurements of PL spectra, as it is necessary to have thin flakes on top of the implantation spot in order to determine the correlation between the NV centers and graphene. After some practice, it became possible to know in which region the flakes will be created. Since the tape deposition does not allow placing of monolayer graphene unless the random chance allows it, it was necessary to use ultrasonic bath for just 3-5 seconds (sometimes multiple times consecutively), in order to remove the layers on top that are tied to each other by weak Van der Waals forces to achieve as few layers as possible.

The final sample used for the main measurements was a diamond substrate of size 2 mm×2 mm. Sample was first cleaned according to the cleaning procedure mentioned above and then implanted with nitrogen ions on several spots. The sample was already used prior to this work, but it sustained no change in terms of its structure and properties. On one half of the sample there are graphitization

marks from the previous work done on it. The other half was used for the purposes of this experiment. Next step was the ion implantation. The nanoimplanter setup was used.

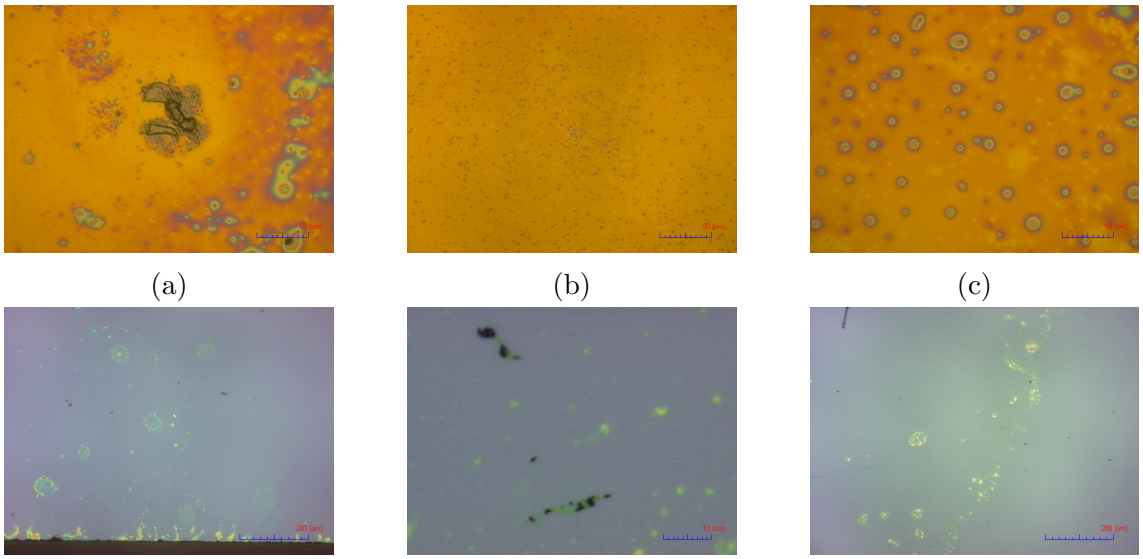

(a) (b) (c)

(d) (e) (f)

Figure 3.4: Si_3N_4 substrates with dirt and evaporation marks after using the graphene solution as deposition method are shown in (a), (b) and (c). SiO_2 substrates with dirt and evaporation marks after using graphene solution are shown in are shown in (d) and (f). In (e) the deposition of carbon nanotubes provided by José Barzola Quiquia, the Academic Assistant in the Superconductivity and Magnetism Division of the Felix Bloch Institute for Solid State Physics of the University of Leipzig, at the time, is shown. All images were taken with the optical microscope and are scaled in the lower right corner showing the magnification used. It is evident that the surfaces are unsatisfactory. Note, carbon nanotubes were used just as a part of the training.

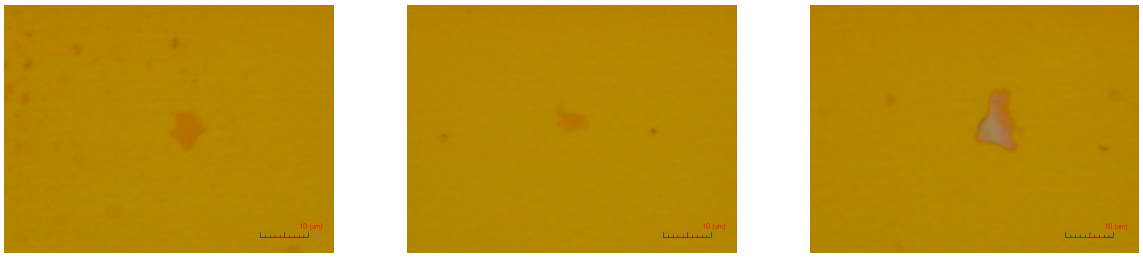

Figure 3.5: Images of good, few-layered flakes of graphene on Si_3N_4 substrates under the optical microscope. The differences in colors show the layers as it goes from almost transparent for just a few layers towards grey for many layers representing graphite.

3.2 Ion Implantation

3.2.1 Nanoimplanter

A home-built nanoimplanter, made by the Advanced Quantum Systems department of the University of Leipzig was employed for the implantation of nitrogen ions in a diamond target. The sketch of the setup can be seen in the Figure 3.6. The procedure takes place inside a high vacuum chamber (see Figure 3.7) with the pressure on the order of 10^{-6} mbar. The ions were produced in a low-kinetic-energy ion source (SPECS IQE 12/38) connected to a nitrogen gas supply as the source of $^{14}N^{+}$ ions. The energy range is from about 0.5 keV to 5 keV. The ions leaving the source pass an aperture with adjustable diameter from 5 µm to 1.25 mm and are focused onto the target using an electrostatic Einzel lens, [41]. There is an additional aperture after the Einzel lens with a diameter of 600 µm for suppressing the outer ions. The sample is positioned on a controllable, integrated X-Y piezo stage with an integrated Faraday cup for the current monitoring. The piezo stage itself is mounted onto another stage driven by the stepper motors for coarse positioning. All areas of the sample holder can be reached this way.

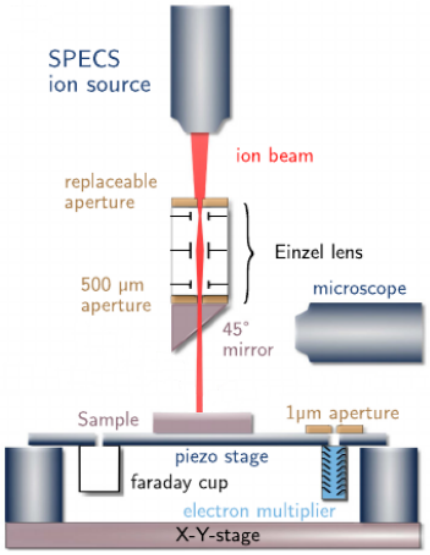

Figure 3.6: The sketch of the Nanoimplanter function principle inside the vacuum chamber used for this experiment, [41].

This setup, additionally, has an AFM system for high-resolution ion implantation from a company nano analytik GmbH and a silicon nitride AFM tip movable in all three directions by a piezo stage. A self-made microscope including a charge-coupled device (CCD) camera and a 45° mirror that allows for the alignment of the beam and the AFM tip, [9, 41]. However the AFM tip was not used in this work because a very precise implantation was not required.

3.2.2 Implantation procedure

The procedure was done at the pressure of 9.23×10^{-6}mbar, with 6.31 mA current on the source and 15 µA current on the first aperture. The implantation was done on

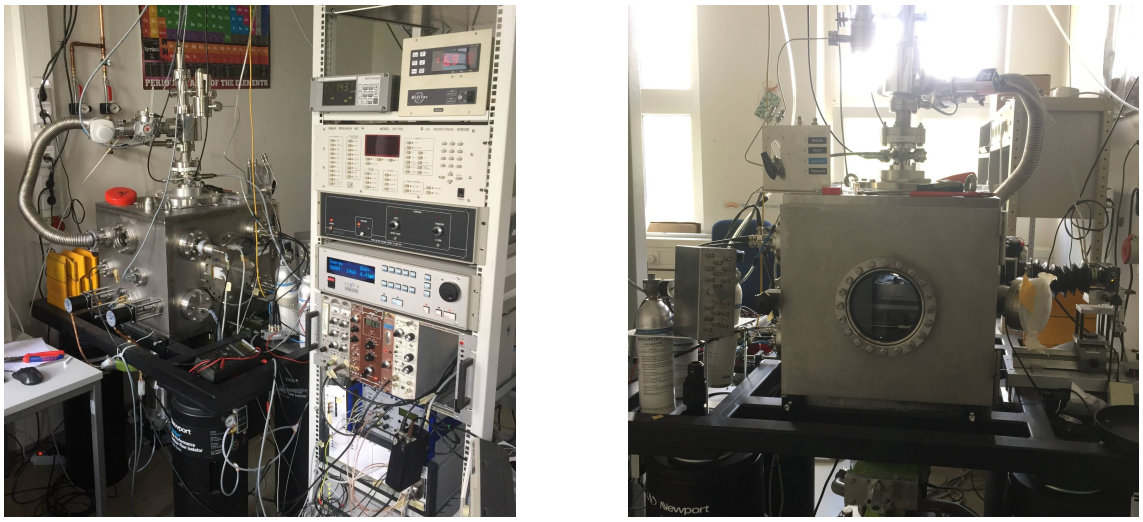

Figure 3.7: Images of the Nanoimplanter setup used at the University of Leipzig.

several spots on the free half of the sample with two different ion energies (2.5 keV and 5 keV) and fluences varying from 10^{10} to 10^{13} ions (see Figure 3.8).

However, only two of the implantation spots (the two spots on the upper left in the Figure 3.8) were visible under the confocal microscope, the 2.5 keV energy and 5 keV energy spots, both with the dose of 10^{13} ions. Although both visible, only the one with the highest energy and dose was used in the following measurements of the fluorescence of NV centers. Implantation spot size was about 600 µm in diameter.

Following the implantation procedure the annealing was done in the high temperature oven at the temperature of 800 °C for 6 hours.

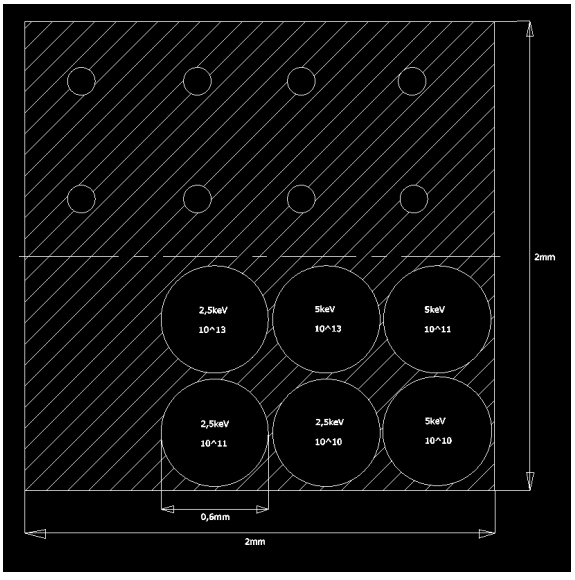

Figure 3.8: The sketch of the diamond sample with small unshaded circles representing the graphitization spots from before, and with big circles representing the implantation spots with energies and doses used written inside of each. Shaded region represents the surface of the sample.

3.2.3 High temperature oven

This machine is a heating chamber made of graphite that can withstand temperatures of up to 2000°C. The whole set consist of a heavy, metal chamber with the graphite heating chamber inside, in which the sample is placed. There is a small lid for the graphite chamber, and a big metal cap with a rubber band on the lower side to prevent the air from entering the structure. There is a vacuum pump that reduces the pressure to about 10^{-6} mbar in order to prevent any oxidation of the diamond at high temperatures. See Figure 3.9.

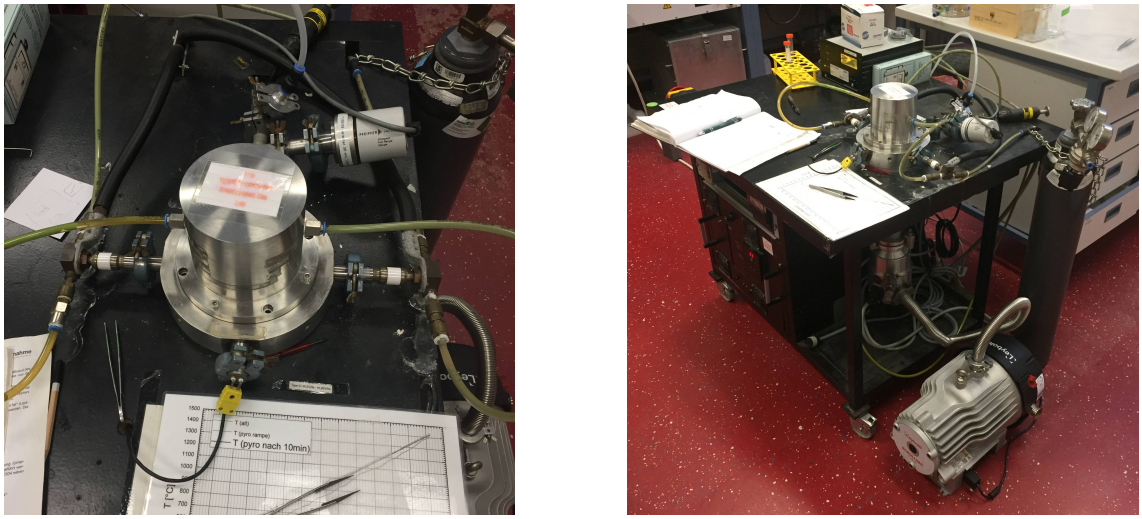

Figure 3.9: The high temperature oven used for the annealing and restructuring of the diamond sample after ion implantation. The images show the setup of the oven with the lid closed. Sadly, at the time when the images were taken, the oven was in use so it was not possible to show what it looks like from the inside.

3.2.4 SRIM simulation

The ion implantation was accordingly simulated using Stop and Range of Ions in Matter (SRIM) software. The simulation was done using TRIM setup for monolayer collision steps with surface sputtering. Nitrogen atoms with atomic number 7, atomic mass 14.003 amu and two energies 2.5 keV and 5 keV impinging on a diamond layer (density 3.51 g cm^{-3}) of widths 150 Å and 300 Å, respectively, were simulated (see Figure 3.10).

The simulations show the expected penetration depths to be 4.5 nm for 2.5 keV ion energy and 8 nm for 5 keV ion energy, with target vacancies created of about 29 vacancies/ion and 50 vacancies/ion, respectively.

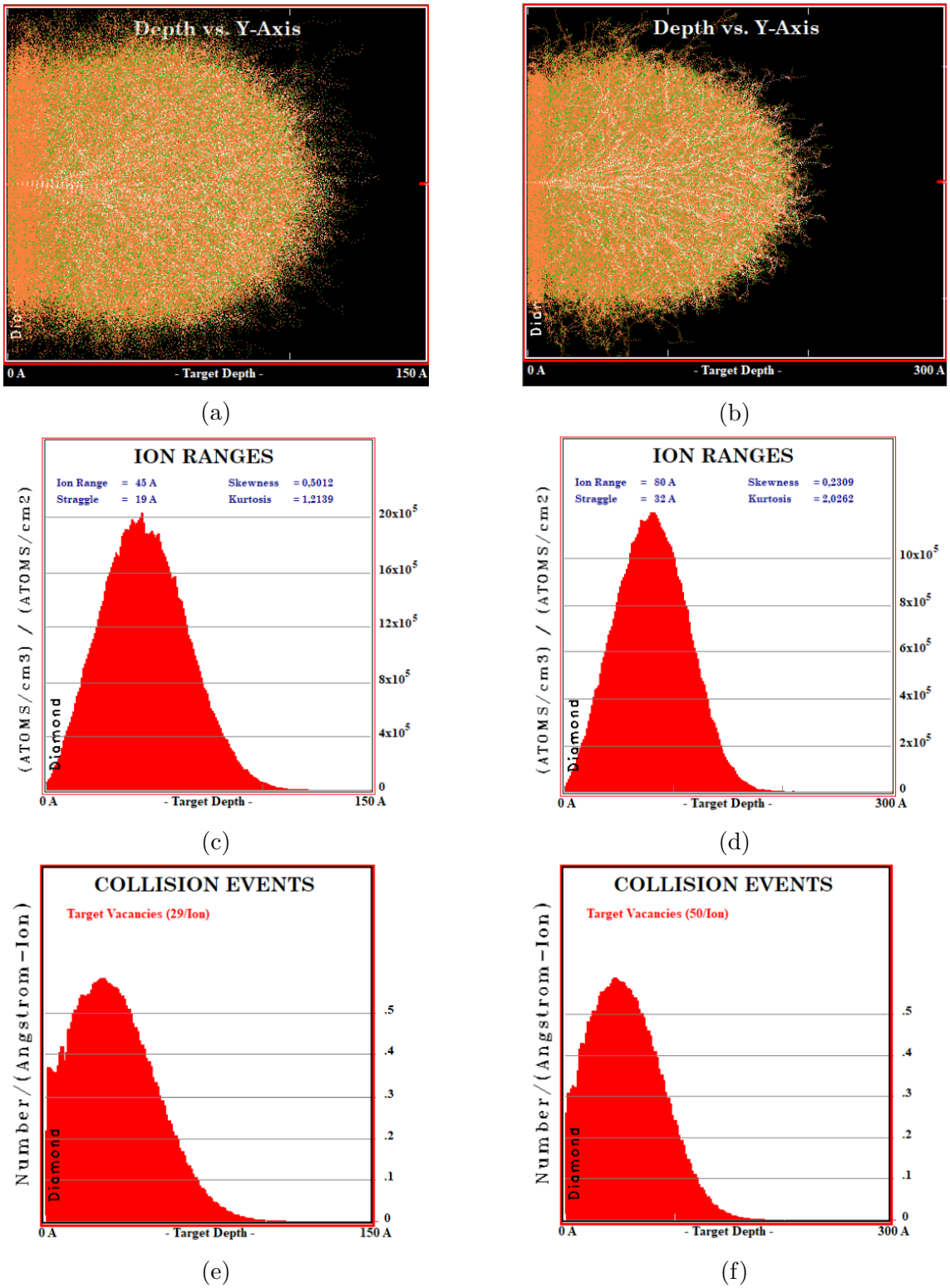

Figure 3.10: The 2.5 keV implantation simulation can be seen in images (a), (c) and (e), while (b), (d) and (f) show the 5 keV implantation. (a), (b) Lateral view of ions impinging the lattice. (c), (d) The ion range in the target, showing the penetration depth of the ions. (e), (f) Show the expected damage done to the target.

3.3 Confocal Microscopy Setup

In order to obtain high resolution images of the sample, a confocal laser scanning microscope (CLSM) was used for the examination of the fluorescence of the NV centers with and without graphene.

3.3.1 Function principle

The biggest difference between a confocal microscope and a regular light microscope is that there is an additional aperture in the form of a pinhole, in the intermediate image plane and thus in the conjugated object plane of the microscope. This arrangement allows for only the light that passes through the pinhole to contribute to the formation of the image, which means that only a very small volume around the focal point on the sample reaches the detector. This creates very high contrast on the image. Since the light is only detected point by point, the movable sample stage is imminent. The sample is scanned by the laser beam point by point to create the full image which often takes some time depending on the resolution desired. See figure 3.11.

The resolving power of a confocal microscope is described by its illumination and detection volume [44, 42], both of them being point-spread functions, h_{ill} and h_{det}. Combined they give the the point-spread function of the additional confocal aperture mentioned above, h_G:

$$h_{\text{G}} = h_{\text{ill}} \times h_{\text{det}}. \tag{3.1}$$

The lateral and axial resolution of the confocal microscope can then be writen as:

$$r_{\text{lateral}} = \frac{0.64\lambda}{\text{NA}}, \quad r_{\text{axial}} = \frac{1.5n\lambda}{(\text{NA})^2}. \tag{3.2}$$

where NA is the numerical aperture of the objective, λ is the wavelength of light used to excite the sample and n is the refractive index. The lateral resolution is just the Rayleign limit. This leads to the definition of the κ geometric factor which represents the ratio of the axial resolution versus the lateral resolution. Then, κ has the form

$$\kappa = \frac{2.33n}{\text{NA}} \tag{3.3}$$

as the lower limit. This factor is important because it describes the confocal volume or the "in-focus" volume within the sample that is efficiently detected with confocal optics. This volume is given by the formula

$$V_C = \pi^{3/2}\kappa w^3 \tag{3.4}$$

where w is the $1/e^2$ beam radius in the xy plane. In principle, the confocal volume is an oblate ellipsoid with κ, the ratio of the length of the major axis to that of the minor axis.

These equations do not take into account the possible light refraction of the beam within the sample which might result in the shift of the focal point on the sample.

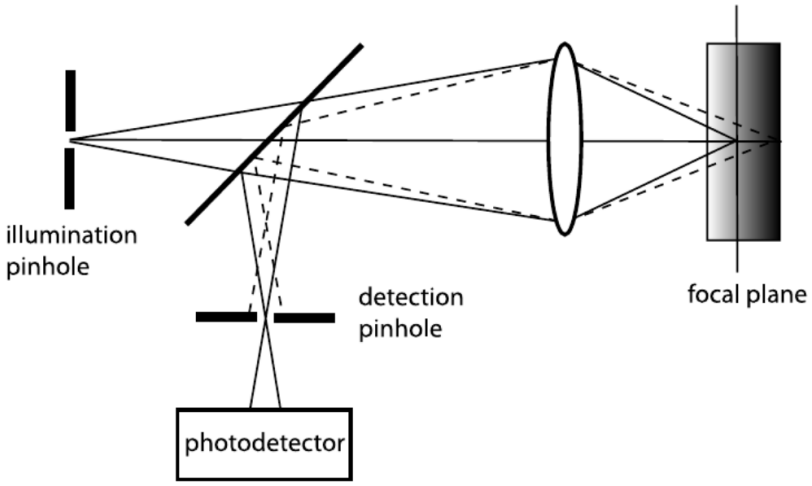

Figure 3.11: From [45], schematic representation of the confocal optical system, showing how the light that is in the focal plane of the object passes through the pinhole completely, while the light from regions of the object lying in planes out of focus arrives at the pinhole defocused and gets blocked from reaching the detector. Which means that only the plane that is in focus gets measured on the detector, resulting in high contrast and resolution of the image.

3.3.2 Measurement setup

The schematic structure of the confocal microscope used can be seen in the Figure 3.12. The whole setup sits on a Newport RS2000™sealed hole table top with tuned damping. A Torus LPQM/Bio green laser with a wavelength of 532 nm is used as the light source for the excitation of the fluorescence of the NV centers. The laser beam from the source first passes through a polarizing beam splitter (PBS, 50-50%) 420 nm to 680 nm into an acusto-optic modulator, AOM. Then the light passes through an optical glass fiber cable reaching the beam expander onto one dichroic mirror. Next in the path, there is another PBS (90-10%) 200 nm to 1100 nm with a monitoring screen used to monitor the power of the laser throughout the measurement as well as to know when the beam is focused on the surface of the sample due to the reflected light from the sample surface, in the preparation for the measurement. Right before the sample stage there is a $\lambda/4$ plate and another 50-50% beam splitter on a gimbal mount (Newport SL51BD). The objective (ThorLabs HCS010) with a 100x magnification and numerical aperture NA= 0.95 focuses the beam on the sample. The sample is positioned on a computer-controlled piezo stage movable in all three directions. The fluorescence from the sample is directed back through the objective and the beam splitter onto a notch filter in order to separate the excitation wavelength from the fluorescence of the sample.

From here, there are two modes of operation of the CLSM. First, it is not shown in Figure 3.12, but to be precise, there are two photodiodes of type SPCM-AQRH from Excelitas that use the avalanche effect (called APD for short) that act as a single-photon counting module (SPCM). In front of one of them there is often a band pass filter that lets only the selected range of wavelength pass through. This allows the combination of two images for the more precise measurement. In principle the APDs can be used to count individual photons with a detection efficiency of maximum

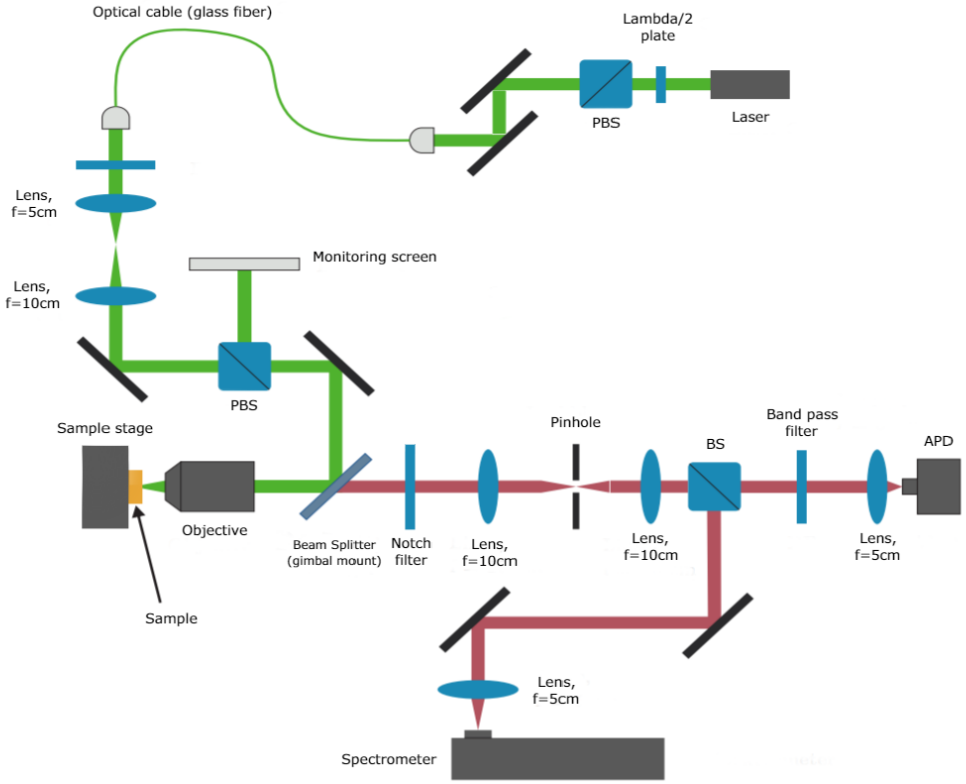

Figure 3.12: Schematic representation of the CLSM function principle used at the University of Leipzig, [42]. The laser beam is shown in *green*, while the fluorescence is in *red*. The *black*, angled rectangular plates represent the mirrors. The sample is shown in *yellow*.

65% at 650 nm wavelength, [43]. The second mode of operation is the spectrometer which can be turned on and off from the computer software, by opening the path that redirects part of the fluorescence onto the spectrometer. It is a CCD-supported spectrometer (Horiba Jobin Yvon GmbH) used for single-point photoluminescence (PL) spectra measurements anywhere within the scan field range.

Finally, for the resolution of the confocal microscope used in this work, following the Equation 3.2 and taking into account the given parameters, the lateral resolution and the axial resolution are

$$r_{\text{lateral}} = 358.4\,\text{nm}, \quad r_{\text{axial}} = 884.21\,\text{nm}. \tag{3.5}$$

with $\kappa = 2.45$.

3.3.3 Confocal measurements

For the confocal (CLSM) measurements, the sample was put on a T-shaped mount placed on the piezo stage. A notch filter 532 nm was placed after the beam splitter on the gimbal mount (see Figure 3.12) in order to attenuate the laser beam wavelength and detect only the fluorescence from the sample. Additionally, since there are two APDs (channel 1 and channel 2), in the beam path in front of one of them (typically, channel 2) a band-pass filter 697/75 nm was used. A setup like this means that only the fluorescence range of 75 nm around the middle point of 697 nm wavelength is

detected (659 nm to 735 nm) on one of the APDs while the full signal arrives on the other. This allows for comparison between the two images.

In order not to burn the graphene flakes it was calculated that the maximum power of the continuous-wave (CW) laser that could be used was about ∼1 mW, and should not be exceeded. For that purpose, the laser power on the order of 500 µ W was commonly used. The power of the laser has a tendency of dropping slightly over time, especially during long measurements, but the changes are overall small and negligible.

The measurements were done using a QUDI software, a python code based program specifically written and adjusted for the system in question. The whole setup is controllable from the software except for the stage approach sequence for which one must be present in person.

For the images under the optical and confocal microscopes of the final flakes of graphene, refer to the Figures 3.13 and 3.14, respectively.

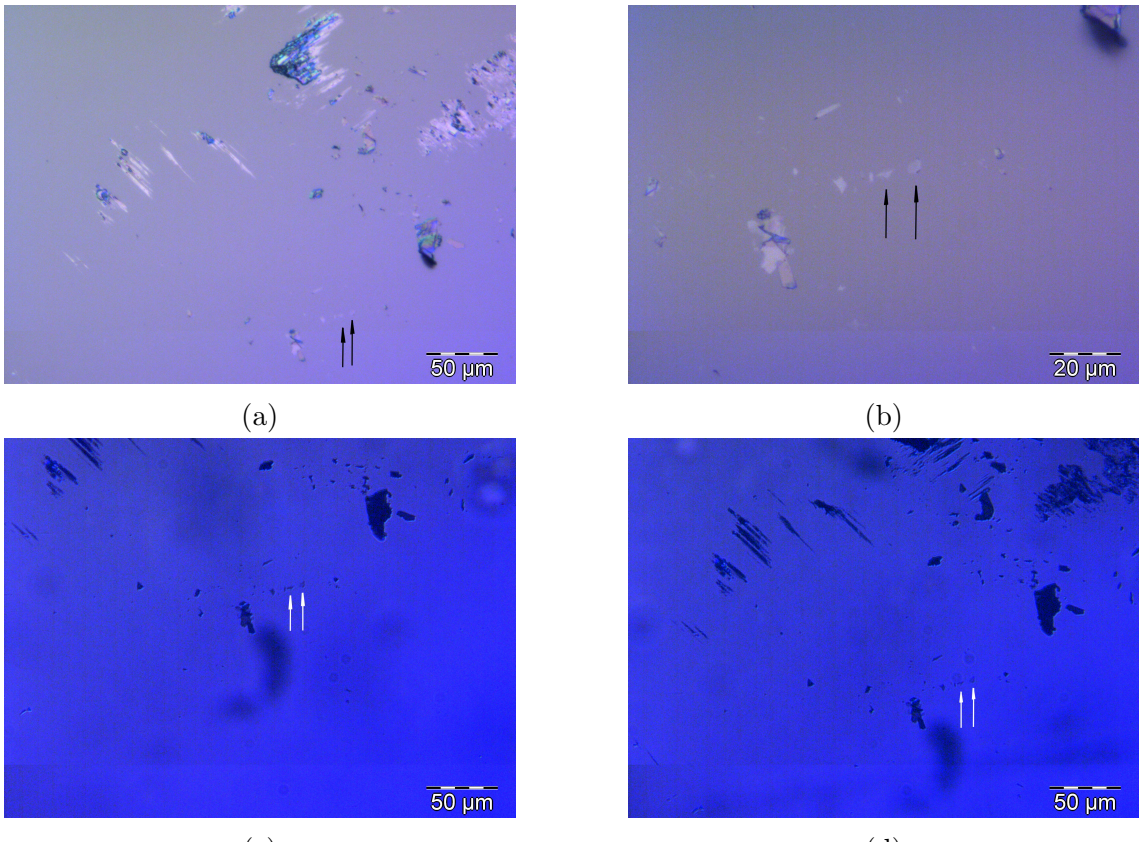

(a) (b)

(c) (d)

Figure 3.13: The images from the optical microscope with light shown from above are presented in (a) and (b), showing the two final graphene flakes positioned on top of the 5 keV with 10^{13} ions implantation spot, where the flake on the right is the main one used for further measurements because of its approximately 2 µm×2 µm area with the same thickness. Note: In (b), a close up view of the same position on the sample as in (a) is shown. The images from the optical microscope with light shown from below of the same two flakes are presented in (c) and (d). Note: (c) and (d) have the same magnification because a close up was not possible due to contrast.

From here, the temperature of the spectrometer was reduced to −60 °C and the spectrometer was employed for the PL measurements. The results of these

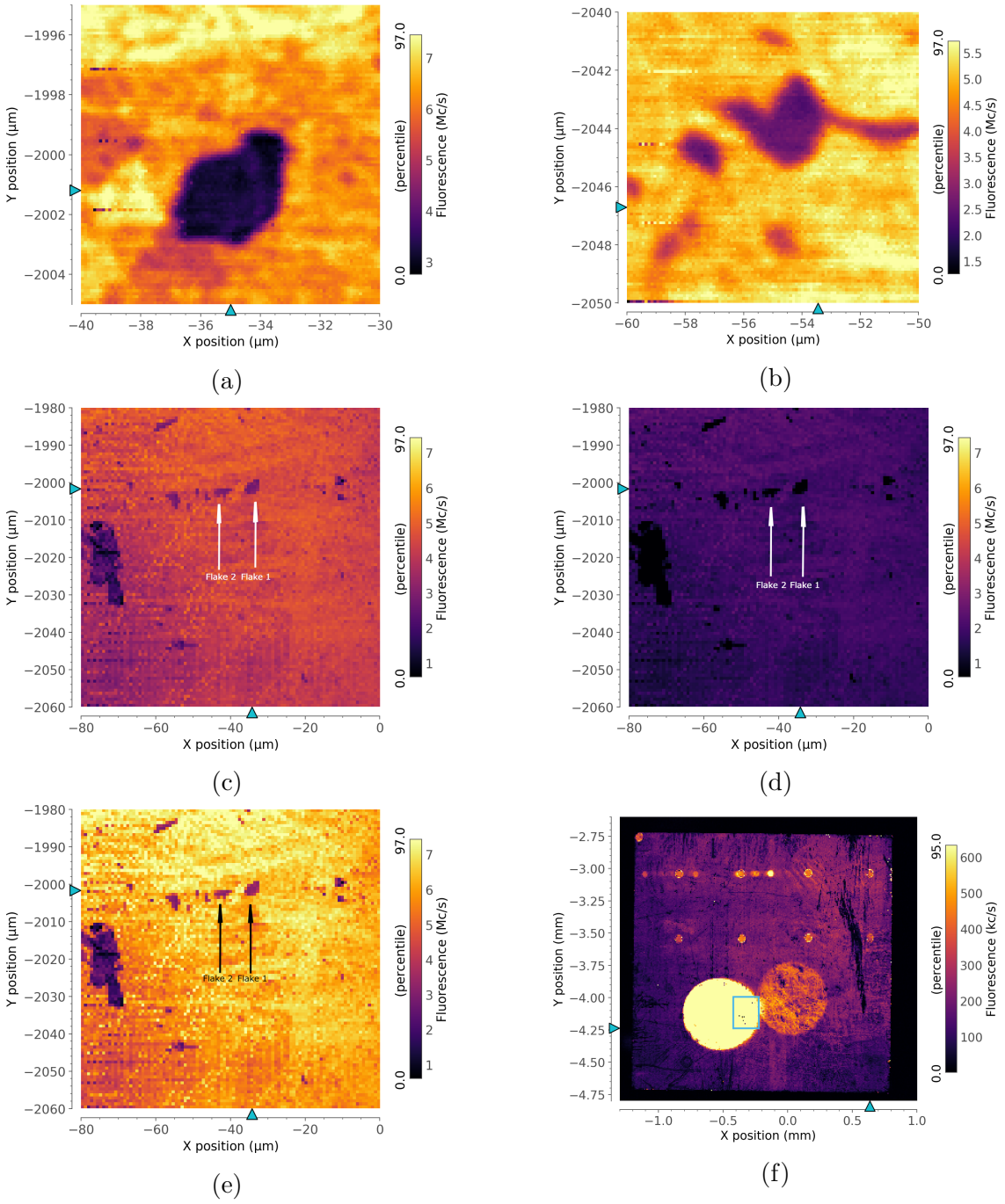

Figure 3.14: Confocal images of the diamond substrate. Flake 1 in (a), the "main" graphene flake. Flake 2 in (b) with less surface area than flake 1. Channel 1, channel 2 and the sum of the two are shown in (c), (d) and (e), respectively, the two flakes are marked by arrows (see Figure 3.13 for comparison). It is evident how channel 2 in (d) has less brightness due to the band-pass filter in front of the APD. An image of the whole sample showing both the graphitization spots made prior to this work as well as only two implantation spots visible in (f) with the region of interest in *blue*. The higher energy implantation is brighter.

measurements and the following fluorescence lifetime measurements are discussed in the next chapter.

3.4 Time-Resolved Fluorescence Lifetime

The fluorescence lifetime is a method used to measure the time a fluorophore takes to return to the ground state by emitting a photon after being initially excited. Return to the ground state is a chain of possible photophysical events, such as internal conversion or vibrational relaxation which represents the loss of energy in the abscence of light emission, fluorescence, intersystem crossing (from a singlet to a triplet state) and phosphorescence. Each of these events has a probability to occur and it can be described using the decay rate constants k. It can be shown that the average lifetime of the excited state is reciprocally proportional to the rate constant, $\tau = 1/k$. Fluorescence lifetime is the time required by a population of N excited molecules to decrease exponentially to N/e through energy loss by fluorescence and other nonradiative processes. These processes occur in a wide range of lifetimes, i.e. from a few femtoseconds for internal conversion to nanoseconds for fluorescence and microseconds or even seconds for phosphorescence [36]. Fluorescence lifetime is an intrinsic property of a fluorophore. Initial perturbation conditions, duration of exposure to light, excitation wavelength or photobleaching do not affect the lifetime. It depends largely on the factors defined by the structure of the fluorophore, as well as the temperature, polarity and the presence of quenchers.

As mentioned above, an excited fluorophore comes back to the ground state through a number of different decay pathways. In order to observe fluorescence, it is important that one of these pathways is a spontaneous photon emission. Then the emitted fluorescence decays with time according to

$$I(t) = I_0 e^{-t/\tau} \tag{3.6}$$

where $\frac{1}{\tau} = \sum k_i$ and t is the time, τ is the fluorescence lifetime, I_0 is the initial fluorescence at $t = 0$ and k_i are the decay constants (or decay rates) for each of the decay paths, [38]. The lifetime τ is independent of the initial intensity and of the emitted light.

3.4.1 Measurement method

Fluorescence lifetime imaging (often referred to as FLIM) results in images where each pixel has an intensity determined by the lifetime τ, which allows viewing contrast between materials even when the wavelength of the fluorescence is exactly the same, or to observe different decay paths as in FRET. FLIM and FRET are aften used as hand in hand techniques.

For FLIM one uses a so called **pulsed illumination**, a population of fluorescent molecules is excited by an ultrashort or delta pulse of light and the time-resolved fluorescence exponential decay is observed, [38]. However, it can be that the excitation pulse or the detection response is wide, which results in a non-purely exponential measured fluorescence decay, $d(t)$. Then the instrumental response function, IRF(t) can be convolved or mixed with the decay function F(t) according to:

$$d(t) = IRF(t) \times F(t). \tag{3.7}$$

The instrumental response of the source, the detector and the instrumentation is usually measured from the scattered excitation light.

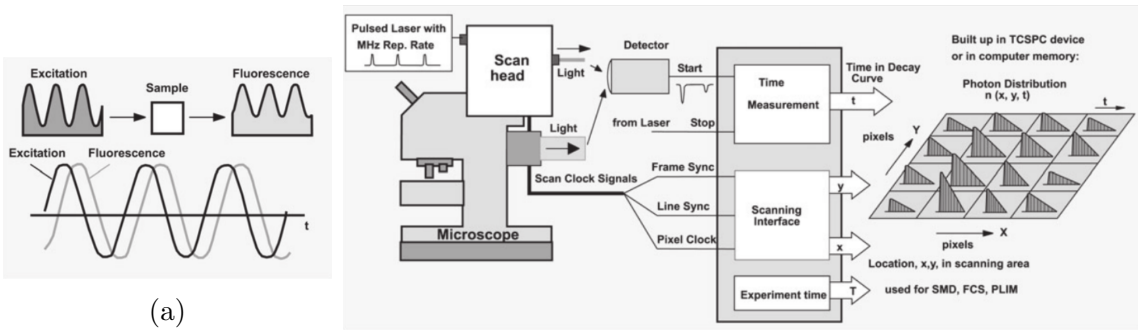

(a) (b)

Figure 3.15: (a) From [39], basic principle of a frequency-domain FLIM. The fluorescence lifetime is extracted from the decrease in modulation degree and the phase shift of the fluorescence compared to the excitation light. (b) From [39], a sketch of the setup used in TCSPC FLIM.

Time-correlated single photon counting (TCSPC) is used in order to compensate for variations in the intensity of the source or the single photon pulse amplitudes. The recorded fluorescence decay histogram obeys Poisson statistics which is used in determining the validity of the fit while fitting. TCSPC records times at which photons are detected using a photomultiplyer tube (PMT) or a single photon avalanche photo diode (SPAD) with respect to the excitation laser pulse. In principle, the sample is excited by modulated or pulsed light, and the fluorescence of the sample has a decreased modulation degree and a phase shift compared to the excitation, see Figure 3.15a, [38, 39]. After multiple laser pulses are recorded, the histogram of the number of events over all of the recorded times is made. Then this histogram can be fitted using an exponential function with the exponential lifetime decay function in question from where the lifetime parameter can be extracted. The basic working principle of a TCSPC FLIM setup can be seen from Figure 3.15b.

3.4.2 Time-resolved fluorescence lifetime measurements setup

In photoluminescence spectroscopy (PL), the sample to be examined is often excited with monochromatic photons. These are typically generated with an excitation laser. In cooperation with M. Sc. Evgeny Krueger from the Semiconductor Physics Group of the University of Leipzig, the room temperature fluorescence lifetime measurements were conducted. In the context of this work a system almost identical to the setup shown in Figure 3.16 was used. It consists of a femtosecond-pulsed TiSa laser (Coherent Mira, 700 nm to 1000 nm, 200 fs, 76 MHz) as the excitation laser. The wavelength of 1000 nm was used. The laser beam passes through a pulse picker (Pulse Select APE), an electrically controlled optical switch used to extract a single pulse from a fast pulse train, with a division ratio of 30. Followed by a BBO crystal that cuts the wavelength in half in order to have the excitation wavelength of 500 nm, and a neutral density filter used for the control of the laser power as needed. The power used in this work was the maximum power of the laser of µW.

Excitation beam then passes through the objective (Mitutoyo M plan Apo NIR 100x) with a numerical aperture of NA= 0.7 resulting in a spot size of the excitation laser on the target of about 2 µm. Next in line is the long pass filter 532 nm that

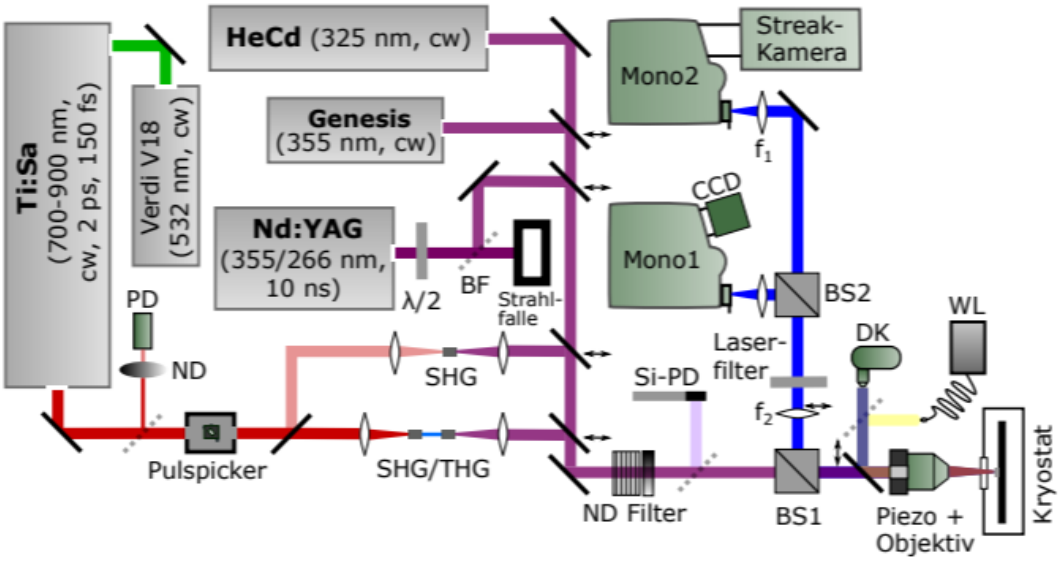

Figure 3.16: The sketch of the Fluorescence lifetime measurement setup used for this experiment, [40].

removes the excitation wavelength and leaves only the fluorescence coming from the target, followed by a beam splitter and a monochromator (Jobin Yvon, iHR320 Horiba, 2400 lines/mm). For lifetime measurements the STREAK camera (Hamamatsu C5680) with a single sweep module M5677 and a CCD detector (CCD C9300 Hamamatsu) was used. For the functioning principle refer to the Figure 3.17. The trigger signal for the STREAK camera is made by the Stanford Research Systems DG645. The time resolution of the lifetime measurements was ∼2.5 ns.

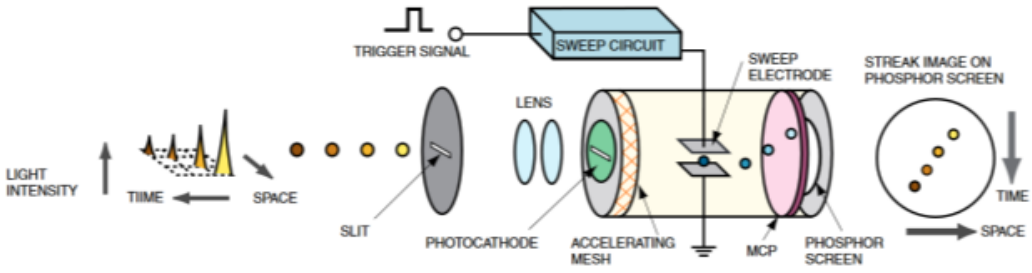

Figure 3.17: The sketch of the functioning principle of the streak camera used for the measurement of the fluorescence lifetime, [40]. Essentially, whenever a photon comes in through the slit it generates an electron which is subjected to the sweeping electric field which then hits the phosphor screen generating an image.

Chapter 4

Results and Discussion

Discussion of the results is presented in this chapter. Starting with the Photoluminescence spectra of graphene flakes and the reference implanted region, discussion of the fitting procedure and the corresponding calculations. Next, the time-resolved fluorescence measurements, the results and the fitting of those are presented followed by the FRET estimation of the coupling between graphene and the NV centers. The data analysis was done using Python and OriginLab.

4.1 Photoluminescence Spectra of Graphene Flakes

Using the spectrometer of the confocal microscope setup yielded results of the photoluminescence spectra at certain spots on the sample. The spectra of the two flakes, mentioned in the last chapter, as well as the reference spectrum of the implantation spot next to the flakes were taken. All of the graphs were then normalized with respect to the diamond Raman peak at 532 nm. There are two reasons for this normalization. Typically, since we are using a 532 nm green laser as the excitation wavelength, the detector reaches saturation at this wavelength. Also, the confocal volume of the laser spot on the sample surface illuminates a certain volume (confocal volume is explained in Chapter 3, Confocal Microscopy). A fraction of this volume is inside the sample while a fraction is still in the air. To eliminate this uncertainty it is best to normalize with respect to the diamond Raman peak. Additionally, the Raman peak is directly proportional to that fraction of the confocal volume.

Subsequently, the data was fitted with the characteristic spectra of NV centers (also normalized with respect to the Raman peak) using a fitting function, y of the form

$$y = A * \mathrm{NV}^0 + B * \mathrm{NV}^- \tag{4.1}$$

where A and B are the coeficients corresponding to the content of NV^0 and NV^-, respectively. It was found that the content of NV centers in each of the measurements was as presented in Table 4.1.

These percentages are useful in the fitting of the time-resolved fluorescence lifetime data.

From Figure 4.1d, the number of layers of the graphene flakes can be calculated according to the work done by R. R. Nair et al. "Fine Structure Constant Defines Visual Transparency of Graphene", [46]. Based on this work, the intensity reduction

	NV^0 (%)	NV^- (%)
Flake 1	35.46	64.54
Flake 2	25.19	74.81
Implantation reference	20	80

Table 4.1: Percentual content of NV centers obtained from the fitted photoluminescence spectra.

of light due to one graphene layer is about 2.3 % and it increases by the same amount for each of the subsequent layers. Following [46] one can solve the equation

$$I_{\text{graphene}} = I \times (0.977)^n \tag{4.2}$$

for n, the number of layers, with I_{graphene} the intensity of the graphene spectra and I the intensity of the reference spectra. The resulting number of layers for flakes 1 and 2 are 21 and 28, respectively.

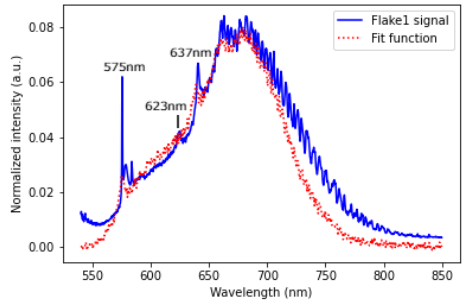

(a) Flake 1

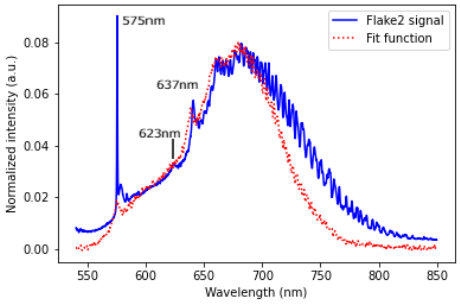

(b) Flake 2

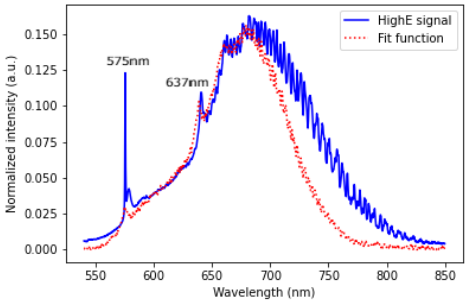

(c) NV reference

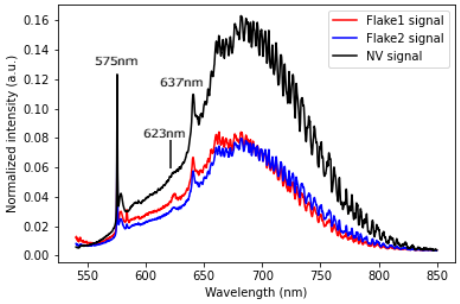

(d) All three spectra

Figure 4.1: (a) Fitted data of the graphene flake 1 spectrum (refer to Figure 3.14a). (b) Fitted data of the flake 2 spectrum (refer to Figure 3.14b). (c) Fitted data of the implantation spot reference spectrum taken next to the flakes. (d) All three spectra on the same graph, the absorption of light from graphene is evident from the difference in the intensity. Note, on all figures, the corresponding NV^0 and NV^- ZPLs are marked showing the wavelength at which the ZPL occurs. In (a) and (b) the position of the 2D peak of characteristic for graphene is also marked. Although, very small, the peak is visible.

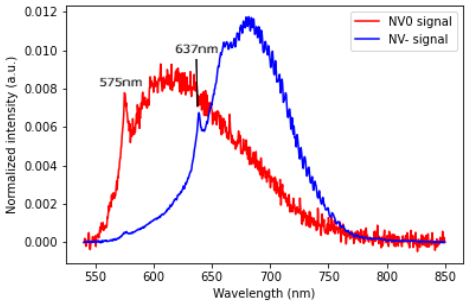

Figure 4.2: Characteristic spectra of the two NV charge states used for the fitting of the data shown in Figure 4.1, with the ZPL wavelengths marked.

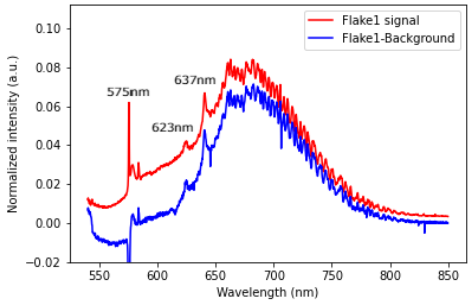

(a) Flake 1

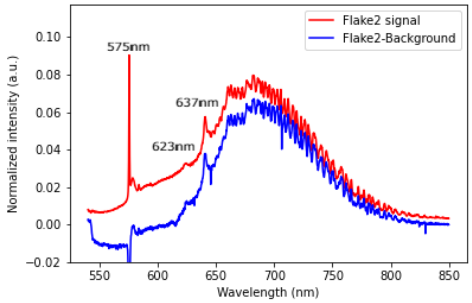

(b) Flake 2

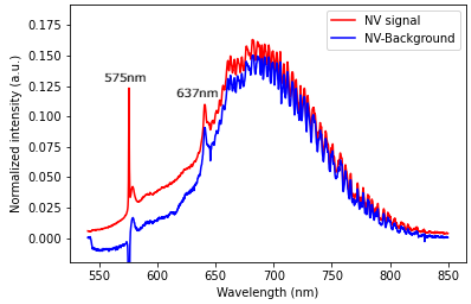

(c) NV reference

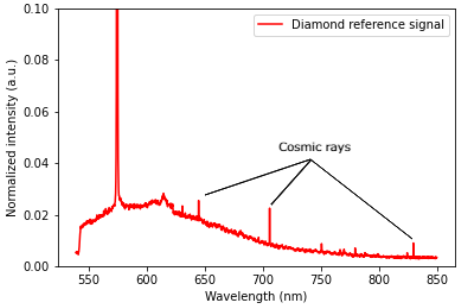

(d) Diamond reference

Figure 4.3: (a), (b) and (c) show spectra of the graphene flakes versus the spectra after the diamond refernce was subtracted. In (d), diamond reference spectrum is shown. The very sharp and sort of random peaks in (d) are the so called cosmic rays (random particles hitting the detector that do not really correspond to the actual spectrum of the sample). Note, on all figures, the corresponding NV^0 and NV^- ZPLs are marked showing the wavelength at which the ZPL occurs. Additionaly, (a) and (b) show the position of the 2D graphene characteristic peak.

The descrepancy between the fits and the PL spectra that are visible in Figure 4.1 could be due to some reflections inside our CLSM setup. There are many factors that could result in this kind of mismatch in the farther part of the phonon sideband, out of which the main reason could be that the measured data and the data used for fitting were not take on the same day. But, it is evident that in the region of smaller wavelength, data fits reasonably well.

4.2 Time-Resolved Fluorescence Lifetime Analysis

For the time resolved measurements, the maximum power of the excitation laser was used. The laser wavelength was 500 nm with the power of 11 µW. At this point it was important not to exceed a certain power density in order not to burn the flakes, but as it turns out, the maximum laser power is far weaker than the threshold for graphene. Knowing that the maximum CW laser power that graphene can withstand is about 1 mW, with the flake diameter of approximately 3 µm, the power density on the spot of that size should not exceed 1.4154×10^{-4} W/cm^2. The maximum power density the laser could provide was 1.5569×10^{-6} W/cm^2.

Overall, the setup was good for a variety of measurements which did not include the one done in this work. It turns out that the laser power was rather weak for the excitation of the fluorescence of the NV centers giving inconsistent and altogether weak signal results. The measurements were a subject to multiple problems constantly. The optimization of the laser and the fluorescence was exceptionally hard. Sometimes it took several hours just to optimize the laser and to have any signal from the sample. Since the signal was so weak, multiple runs of the same settings were done and then combined in order to have a higher signal in the end. Sometimes, the laser power would drop or the pulse would change, resulting in a failure. Also, vibrations from the surroundings, like people walking by, would change the settings of the laser and it would shut down. All in all, it was challenging and it makes one question the validity of the results. Because of all these obstructions, the measurements were taken in runs of 30-60 minutes, usually 4 or 5 of them and then the results were combined. However, as it will be evident from the further discussion, even the combined ones did not yield very good results.

In all of the following measurements the lifetime range used was 100 ns with the time resolution of 2.5 ns. The data was fitted with exponential functions, both mono-exponential and bi-exponential. Mono-exponential fitting functions were used for all the fits, both the data integrated over the whole range of wavelength as well as integrating over the first half and the second half (first half 550 nm to 650 nm for the mainly NV^0 centers and second half 650 nm to 800 nm for mostly NV^- centers). The bi-exponential fitting was primarily used for data integrated over the full range of wavelengths as it involves both charge states of NV centers and here the comparison is made between the fits using the percentages from the Table 4.1, and the fits without these. The mono-exponential used is of the form

$$y_{\text{mono}} = y_0 + A_1 \exp\left(-\frac{x}{t_1}\right) \tag{4.3}$$

with three parameters, while for the bi-exponential

$$y_{\text{bi}} = y_0 + A_1 \exp\left(-\frac{x}{t_1}\right) + B_1 \exp\left(-\frac{x}{t_2}\right) \tag{4.4}$$

with five parameters. In these equations t_1 and t_2 are the lifetimes, A and B are the amplitudes and y_0 is the offset. The goal was to reduce the chi-squared (χ^2) value until the fit converges. This process is called the *deconvolution of fluorescence decay profiles*. In practice, the excitation pulse is not a δ-function and the instrumentation has an electronic response time quantified by the so called IRF (instrument response

function). If the excitation pulse is assumed to be a series of δ-functions with varying amplitudes then the Intensity at time t, $N(t)$ has the form

$$N(t) = \int_0^t IRF(t'_\delta) I(t - t'_\delta) dt' \tag{4.5}$$

where $I(t - t'_\delta)$ stands for the fluorescence intensity at time t, as a response to a δ-excitation pulse at time t' with amplitude $IRF(t)$. This equation is called the convolution integral and the goal is to find a profile $I(t)$ such that it gives the best overall fit between $N(t)$ and $IRF(t)$. This is achieved with the iterative reconvolution with least squares analysis minimizing the χ^2 parameter that represents the "goodness-of-fit". Chi-squared contains the squared differences between all measured data points and the modeled decay

$$\chi^2 = \sum_{i=1}^{n} \left[\frac{\text{actual deviation}}{\text{expected deviation}} \right]^2 \times \frac{1}{n} = \left[\sum_{i=1}^{n} \frac{(N(t_i) - N_c(t_i))^2}{N(t_i)} \right] \times \frac{1}{n} \tag{4.6}$$

where $N(t_i)$ is the measured intensity at time t_i, $N_c(t_i)$ is the modeled intensity at time t_i and n is the number of data points. The "goodness-of-fit" is described by the value of χ^2 close to 1 and the weighted residual between the measured and the calculated decay curve should be randomply distributed around 0.

4.2.1 Measurements without graphene

Two measurements without graphene are presented here. The difference between them is in the exposure time and the wavelength range recorded for each of the runs. Both consist of four runs combined, with the parameters as follows:

Parameter name (units)	**Measurement 1**	**Measurement 2**
Number of exposures	3956	7200
Exposure time (ms)	500	500
Wavelength range (nm)	548-810	627-890
Central wavelength (nm)	690	770
Grating (g/mm)	50	50
Slit width (µm)	198	198

Table 4.2: Parameters used in the time-resolved measurements of the implantation spot without graphene.

Data from the measurements in Table 4.2 were then fitted using OriginLab with mono- and bi-exponential decay functions integrated in the software. The fitting was done over the whole range of wavelengths, 550 nm to 750 nm for both measurements. Additionally, the wavelength range for measurement 1 (M1) was split into two parts and integrated over 550 nm to 650 nm and 650 nm to 750 nm. For measurement 2 (M2), the wavelength range is already in the far where the overlap of NV^0 and NV^- is evident (refer to Figure 4.2 and Table 4.2).

Note, that the χ^2 values in Tables 4.4 and seem weirdly large. But the χ^2 calculation is directly proportional to the number of degrees of freedom (DOF) for

the measurements, and degrees of freedom were calculated to be on the order of 200 which when put into χ^2/DOF gives a much smaller value. It is because of the way OriginLab calculates this value and gives a separate value of χ^2 and of DOF that this value seems uncontrollably large. However, the software also reports for each fitting when the reduced χ^2 value converges to 10^{-9} that the fit converges, which was the case for all the fits presented below (see Figure 4.4).

Mono-exponential fits

Here, the mono-exponential fits to the measurements 1 and 2 (denoted as M1 and M2) without graphene are presented with all the corresponding information on the parameters, the integrated wavelength range and the error estimation in Tables 4.3 and 4.4, respectively.

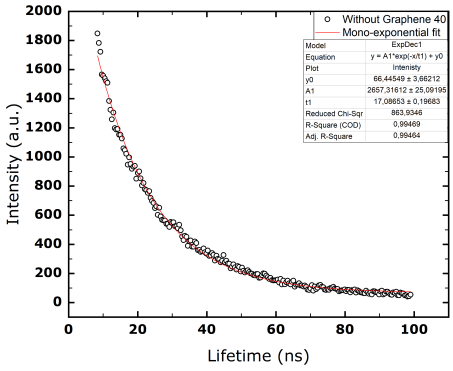

(a) Measurement 1 (550 nm to 750 nm)

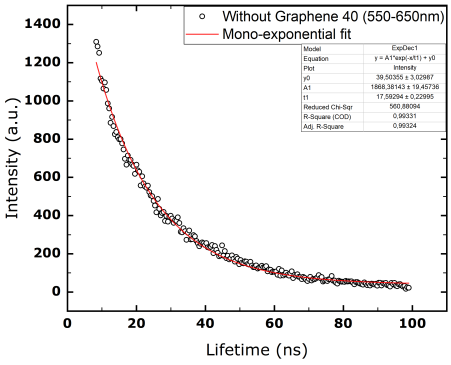

(b) Measurement 1 (550 nm to 650 nm)

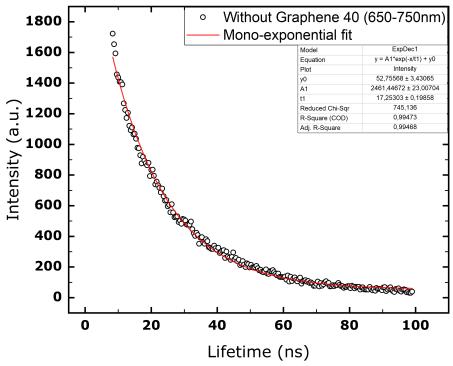

(c) Measurement 1 (650 nm to 750 nm)

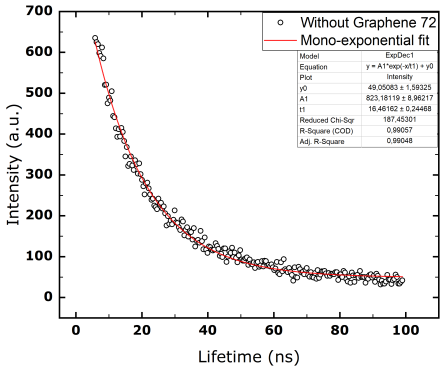

(d) Measurement 2 (630 nm to 830 nm)

Figure 4.4: Mono-exponential fits of the measurements in Table 4.2.

Mono-exponential fit			
Parameter name	**y_0 (a.u.)**	**A_1 (a.u.)**	**t_1 (ns)**
M1 (550-750 nm)	66.445 ± 3.662	2657.316 ± 25.091	17.086 ± 0.196
M1 (550-650 nm)	39.503 ± 3.029	1868.381 ± 19.457	17.592 ± 0.229
M1 (650-750 nm)	52.755 ± 3.431	2461.446 ± 23.007	17.253 ± 0.198
M2 (630-830 nm)	49.051 ± 1.593	823.181 ± 8.962	16.461 ± 0.244

Table 4.3: Fit parameters for mono-exponential fitting of the time-resolved data without graphene.

Mono-exponential fit		
Parameter name	**Reduced χ^2**	**R-Square**
M1 (550-750 nm)	863.934	0.994
M1 (550-650 nm)	560.880	0.993
M1 (650-750 nm)	745.136	0.995
M2 (630-830 nm)	187.453	0.991

Table 4.4: Error estimation values for the mono-exponential fitting of the time-resolved data without graphene.

Bi-exponential fits

Here, the bi-exponential fits to the measurements 1 and 2 (denoted as M1 and M2) without graphene are presented with all the corresponding information on the parameters, the integrated wavelength range and the error estimation in Tables 4.5 and 4.6, respectively.

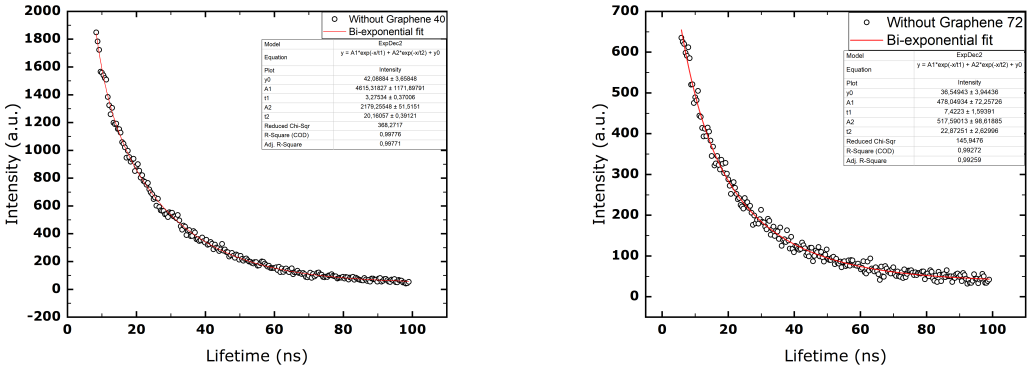

(a) Measurement 1 (550 nm to 750 nm) (b) Measurement 2 (630 nm to 830 nm)

Figure 4.5: Bi-exponential fits of the measurements in Table 4.5.

For this part of the analysis, the values from the Table 4.1 were supposed to be used as amplitudes A_1 and A_2. But sadly, the fits did not make any sense once those values were set as fixed. The software would report a non-converging fit every time. Thus those graphs did not make it as valid here in the analysis.

Bi-exponential fit		
Parameter name	**M1 (550-750 nm)**	**M2 (630-830 nm)**
$\mathbf{y_0}$ **(a.u.)**	42.088 ± 3.658	36.549 ± 3.944
$\mathbf{A_1}$ **(a.u.)**	4615.318 ± 1171.897	478.049 ± 72.257
$\mathbf{t_1}$ **(ns)**	3.275 ± 0.370	4.422 ± 1.594
$\mathbf{A_2}$ **(a.u.)**	2179.255 ± 51.515	517.590 ± 98.618
$\mathbf{t_2}$ **(ns)**	20.161 ± 0.391	22.872 ± 2.629

Table 4.5: Fit parameters for bi-exponential fitting of the time-resolved data without graphene.

Bi-exponential fit		
Parameter name	**M1 (550-750 nm)**	**M2 (630-830 nm)**
Reduced χ^2	368.271	145.947
R-Square	0.997	0.993

Table 4.6: Error estimation values for the bi-exponential fitting of the time-resolved data without graphene.

4.2.2 Measurement with graphene

Even though there were two flakes as mentioned in the beginning of this chapter, here only the results from flake 1 will be presented. Due to a lack of time, it was not possible to collect the data for flake 2. Although the fits are appropriately made, the findigs are not consistent with the expectations. The reson for such inconsistency is the low power of the laser and thus the low yield of fluorescence intensity. Also, the absorption of graphene in this work is quite high because of the large number of layers which significantly reduces the measured fluorescence intensity. In Table 4.7, the parameters of the measurement are shown.

Parameter name (units)	**Flake 1**
Number of exposures	4152
Exposure time (ms)	500
Wavelength range (nm)	548-810
Central wavelength (nm)	690
Grating (g/mm)	50
Slit width (µm)	198

Table 4.7: Parameters used in the time-resolved measurement of the implantation spot with graphene flake 1.

Data from Table 4.7 was then fitted using OriginLab with mono- and bi-exponential decay functions integrated within the software. The fitting was done over the full range of wavelengths with both exponential fits, as well as with mono-exponential fit for the integration over the first 550 nm to 650 nm part and the second 650 nm to 750 nm part. The parameters used in the fits are shown in Tables 4.8, 4.9 and 4.10

while the graphs can be seen in Figure 4.6.

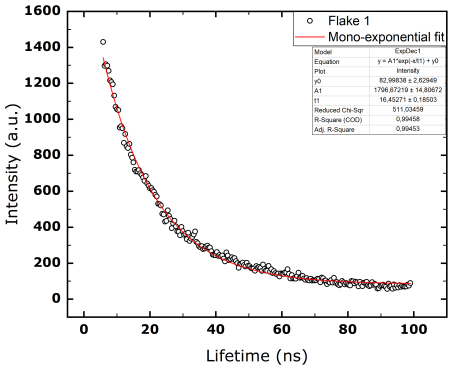

(a) Mono-exponential fit for flake 1 (550 nm to 750 nm)

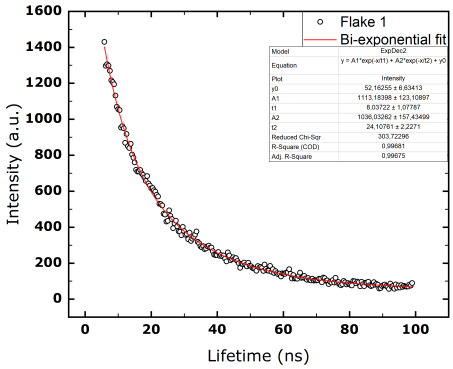

(b) Bi-exponential fit for flake 1 (550 nm to 750 nm)

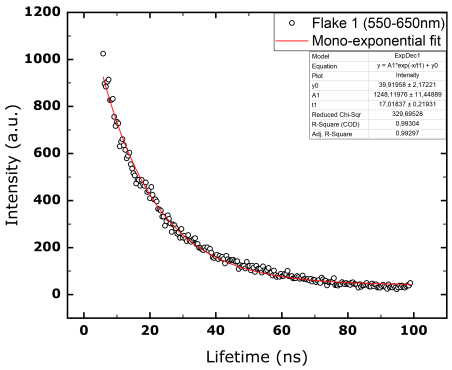

(c) Mono-exponential fit for flake 1 (550 nm to 650 nm)

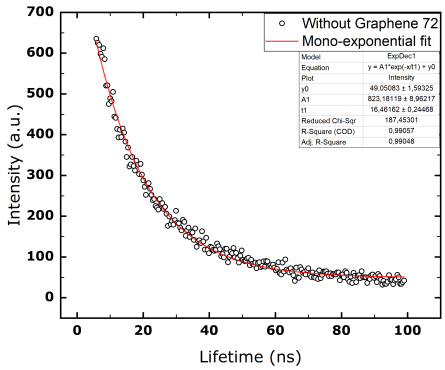

(d) Mono-exponential fit for flake 1 (650 nm to 750 nm)

Figure 4.6: Fitting of the data from the measurement with the graphene flake 1, shown in Table 4.7.

Mono-exponential fit			
Parameter	**y_0 (a.u.)**	**A_1 (a.u.)**	**t_1 (ns)**
Flake 1 (550-750 nm)	82.998 ± 2.629	1796.672 ± 14.806	16.452 ± 0.185
Flake 1 (550-650 nm)	39.919 ± 2.172	1248.119 ± 11.448	17.018 ± 0.219
Flake 1 (650-750 nm)	57.895 ± 2.446	1645.500 ± 13.419	16.675 ± 0.187

Table 4.8: Fit parameters for mono-exponential fitting of the time-resolved data with graphene flake 1.

Mono-exponential fit		
Parameter	**Reduced χ^2**	**R-Square**
Flake 1 (550-750 nm)	511.034	0.994
Flake 1 (550-650 nm)	329.695	0.993
Flake 1 (650-750 nm)	432.749	0.994

Table 4.9: Error estimation values for the mono-exponential fitting of the time-resolved data with graphene flake 1.

Bi-exponential fit	
Parameter name	**Flake 1 (550-750 nm)**
$\mathbf{y_0}$	52.162 ± 6.634
$\mathbf{A_1}$	1113.183 ± 123.108
$\mathbf{t_1}$	8.037 ± 1.077
$\mathbf{A_2}$	1036.032 ± 157.435
$\mathbf{t_2}$	24.107 ± 2.227
Reduced χ^2	303.723
R-Square	0.997

Table 4.10: Fit parameters for the bi-exponential fitting of the time-resolved data with graphene flake 1 (see Figure 4.6b).

4.3 Discussion and FRET Estimation

Based on the research about the FRET mechanism, one could expect a reduction in the lifetime of NV centers in the presence of graphene compared to the lifetime in the absence of graphene, in the range of about 2 ns to 4 ns. However, in this work that was not observed. In Tables 4.11 and 4.12, one can see and compare the lifetime values from the fits presented in the previous section in the presence and absence of graphene.

Mono-exponential fits	
τ_{DA} (ns)	τ_{D} (ns)
16.452 ± 0.185	17.086 ± 0.196
17.018 ± 0.219	17.592 ± 0.229
16.675 ± 0.187	17.253 ± 0.198
—	16.461 ± 0.244

Table 4.11: Comparison of lifetimes in the presence τ_{DA} and in the absence τ_{D} of graphene for the mono-exponential fit. Note, in the presence of graphene there were three measurements while in the absence there were four because graphene flake 2 was not regarded.

Here, it is observed that for the mono-exponential fits there is almost no change of lifetime related to the presence and absence of graphene. To be exact, the average of the lifetimes observed in the presence of graphene is $\tau_{\mathrm{DA}} = 16.715 \pm 0.197$ ns

Bi-exponential fits			
NV^0		**NV^-**	
τ_{DA} (ns)	τ_D (ns)	τ_{DA} (ns)	τ_D (ns)
24.107 ± 2.227	20.161 ± 0.391	8.037 ± 1.077	3.275 ± 0.370
—	22.872 ± 2.629	—	4.422 ± 1.594

Table 4.12: Comparison of lifetimes in the presence τ_{DA} and in the absence τ_D of graphene from the bi-exponential fit for NV^0 and NV^-, respectively. Note, in the presence of graphene there was only one measurement and in the absence there were two because flake 2 was not regarded.

while the average in the absence is $\tau_D = 17.098 \pm 0.217$ ns. This result shows a reduction in the lifetime of 0.383 ± 0.405 ns which is very short and given the time-resolution of the setup of 2.5 ns for the time-resolved measurements, it is insufficient to conclude whether FRET actually occurs. However, for the bi-exponential fits, the observation shows an increase in the lifetime of both NV^0 and NV^- centers in the presence of graphene, which is contradictory to the expectation. For NV^0, the increase in lifetime in the presence of graphene is about 2.591 ± 3.164 ns, where for NV^- that increase is around 4.189 ± 3.124 ns. Additionally, the result for the NV^- in the absence of graphene is far too short compared to the known value, while this value in the presence of it is very close to what one would expect.

All in all, the measurements yield questionable, inconsistent results, that cannot be used for the estimation of FRET as they do not satisfy the condition for the reduction of lifetime in the presence of the acceptor.

Chapter 5

Summary and Conclusion

This research aimed to find the correlation between the nitrogen-vacancy centers implanted in a diamond substrate and a graphene layer on top of the implantation through the principle Förster resonance energy transfer. A diamond substrate was first cleaned and implanted with $^{14}N^{+}$ ions with different energies and doses. The implantation results were then imaged on the confocal microscope followed by graphene deposition using the sticky tape method. After that, photoluminescence spectra of the implanted region and deposited graphene were taken and the time-resolved fluorescence lifetime measurements of the region of interest were performed.

However, the overall results were inconsistent, showing little to no correlation between the two atoms. The expectations were not met and the interpretation of results turned out to be challenging. The excited state lifetime of the nitrogen-vacancy centers showed very small reduction of 0.383 ± 0.405 ns in the presence of graphene in some of the measurements, while the other measured data it was found that the lifetime seemingly increased by about 2.591 ± 3.164 ns for the neutral charge state and by 4.189 ± 3.124 ns for the negative charge state of the color centre. This is a contrary to the expectation as the Förster resonance energy transfer should result in a shorter lifetime of the color centers.

There are several reasons for such findings. First, the tape deposition of graphene proved to be a very inconsistent method of making graphene layers, especially monolayers or few-layered flakes. It is a process that requires experience and time to show good results. The final flakes used as graphene had twenty-one and twenty-eight layers, and were the thinnest flakes observed during the whole process of this work. The other obstacle was with the time-resolved fluorescence lifetime measurements setup, which was not optimal for the purpose of this experiment. The maximum power of the excitation laser was still too weak to produce good signal to noise ratio of the fluorescence from the sample. Even after many attempts to optimize the laser path and the power, the signal was still too weak. Additionally, this could be further explained through the number of layers the graphene used consisted of. The absorption of graphene is quite high with the 2.3 % light absorption per layer which means that with the flakes that were used, only about 61 % of the fluorescence signal reached the detector.

For future work on this topic it would be beneficial to try out a different approach. Beginning with the graphene deposition, using a different, more consistent method of forming graphene monolayers would be a good place to start. For example, chemical vapor deposition is the most commonly used method of growing graphene monolayers

in recent years. It continuously shows good results when it comes to the thickness and the properties of the layers created. Another idea, would be to further optimize the time-resolved fluorescence lifetime setup, primarily using a stronger laser. An increase by at least one order of magnitude for the power is required in order to achieve significantly better results.

Bibliography

[1] Novoselov, K. S., Geim, A. K., Morozov, S. V., Jiang, D., Zhang, Y., Dubonos, S. V., Grigorieva, I. V., Firsov, A. A.. *Electric Field Effect in Atomically Thin Carbon Films*. Science, Vol. 3067, Pages 666-669, *2004*.

URL: `http://science.sciencemag.org/content/306/5696/666.abstract`

[2] Geim, A. K.. *Graphene prehistory*. Physica Scripta, IOP Publishing, Vol. 146, *2012*.

DOI: 10.1088/0031-8949/2012/t146/014003

[3] Brodie, Benjamin Collins. *XIII. On the atomic weight of graphite*. Philosophical Transactions of the Royal Society of London, Vol. 149, Pages 249-259, *1859*.

DOI: 10.1098/rstl.1859.0013

[4] Boehm, H.P., Setton, R., Stumpp, E.. *Nomenclature and terminology of graphite intercalation compounds*. Carbon, Vol. 24, Pages 241-245, *1986*.

DOI:`https://doi.org/10.1016/0008-6223(86)90126-0`

[5] Y. Tzeng, Y. Chen, P. Li, C. Chang, Y. Chu. *NV Center Charge State Controlled Graphene-on-Diamond Field Effect Transistor Actions With Multi-Wavelength Optical Inputs*. IEEE Open Journal of Nanotechnology, Vol. 1, Pages 18-24, *2020*.

DOI: 10.1109/OJNANO.2020.2993007

[6] Younis Muhammad Rizwan, He Gang, Lin Jing, Huang Peng. *Recent Advances on Graphene Quantum Dots for Bioimaging Applications*. Frontiers in Chemistry, Vol. 8, Pages 424, *2020*.

DOI: 10.3389/fchem.2020.00424

[7] Alonso Calafell, I., Cox, J. D., Radonjić, M., Saavedra, J. R. M., García de Abajo, F. J., Rozema, L. A., Walther, P.. *Quantum computing with graphene plasmons*. npj Quantum Information, Vol. 5, *2019*.

DOI: 10.1038/s41534-019-0150-2

[8] T. Lühmann et al. *Screening and engineering of colour centres in diamond*. J. Phys. D: Appl. Phys.51 483002, Pages 891-921, *2018*.

DOI: `https://doi.org/10.1088/1361-6463/aadfab`

[9] S. Pezzagna and J. Meijer. *High-Resolution Ion Implantation from keV to MeV*. Ion Implantation, IntechOpen, *2012*.

[10] Paul K. Chu. *Ion Implantation*, Chapter 9, Lecture. City University of Hong Kong.

[11] L. Childress, R. Hanson. *Diamond NV centers for quantum computing and quantum networks*. MRS Bulletin 38.2, Pages 134-138, *2013*.

DOI: 10.1557/mrs.2013.20

[12] Charles Kittel. *Introduction to Solid-State Physics.* 8th Edition, *2005*.

[13] Jenö Sólyom. *Fundamentals of the Physics of Solids: Volume 1: Structure and Dynamics.* Vol. 1. Springer Science & Business Media. *2007*.

[14] Steven H. Simon. *The Oxford Solid-State Basics.* OUP Oxford, *2013*.

[15] Ashcroft, Neil W., and N. David Mermin. *Solid state physics [by] Neil W. Ashcroft [and] N. David Mermin. 1976*.

[16] Gion Calzaferri and Ruedi Rytz. *The Band Structure of Diamond.* The Journal of Physical Chemistry, *1996*, 100(26), 11122-11124.

DOI: 10.1021/jp960840t

[17] W. Saslow, T. K. Bergstresser, and Marvin L. Cohen. *Band Structure and Optical Properties of Diamond.* Phys. Rev. Lett. **16**, 354 - Published *28 February 1966*; Erratum Phys. Rev. Lett. **21**, 715 (*1968*).

DOI: `https://doi.org/10.1103/PhysRevLett.16.354`

[18] Steven Prawer and Robert J. Nemanich. *Raman spectroscopy of diamond and doped diamond.* Phil. Trans. R. Soc. Lond. A 2004 **362**, 2537-2565. *December, 2004.* DOI:10.1098/rsta.2004.1451

[19] **elementsix**™.*The Element Six CVD Diamond Handbook*

[20] Alexander M. Zaitsev. *Optical Properties of Diamond: A Data Handbook.* Springer, 2001.

ISBN: 3-540-41448-7

[21] Barnard, Amanda and Russo, Salvy and Snook, I.*Comparative Hartree-Fock and density-functional theory study of cubic and hexabonal diamond.*Volume 82, Philosophical Magazine.*2002*.

DOI: 10.1080/1364281021000041250

[22] Ibach, Harald and Lüth, Hans. *Solid-State Physics: An Introduction to Principles of Materials Science.* Springer, *2009*. Fourth Edition.

e-ISBN: 978-3-540-93804-0

[23] Walker, John. *Optical absorption and luminescence in diamond.* Reports on Progress in Physics. Vol. 42, *1979*. (10): 1605–1659.

DOI:10.1088/0034-4885/42/10/001

[24] Yamamoto, T. et al. *Extending spin coherence times of diamond qubits by high-temperature annealing*. Phys. Rev. B., Vol. 88, American Physical Society, *2013*.

DOI: 10.1103/PhysRevB.88.075206 URL:https://link.aps.org/doi/10.1103/PhysRevB.88.075206

[25] F. Jelezko and J. Wrachtrup. *Single defect centres in diamond: A review*. Phys. stat. sol. (a) **203**, No. 13, 3207-3225, *2006*.

DOI: 10.1002/pssa.200671403

[26] Marcus W. Doherty, Neil B. Manson, Paul Delaney, Fedor Jelezko, Jörg Wrachtrup and Lloyd C.L. Hollenberg. *The Nitrogen-Vacancy Colour Centre in Diamond*. Phys. Rep. Vol. 528, Issue 1, *1 July 2013*.

DOI: https://doi.org/10.1016/j.physrep.2013.02.001

[27] Mikhail I. Katsnelson. *Graphene, Carbon in Two Dimensions*. Materials Today, Volume 10 (*2007*).

DOI: https://doi.org/10.1016/S1369-7021(06)71788-6.

[28] Walicki, S.K. & Enoki, Toshiaki & Rao, C.N.R.. *Graphene and its fascinating attributes*, (*2011*). 10.1142/7989.

[29] Childres, Isaac and Jauregui, Luis A. and Park, Wonjun and Cao, Helin and Chen, Yong P. and others. *Raman Spectroscopy of Graphene and Related Materials*, *2013*. New developments in photon and materials research, Vol. 1, Citaseer.

[30] S. Hartmann, D. Weidlich, D. Klostermeier. *Chapter Eleven - Single-Molecule Confocal FRET Microscopy to Dissect Conformational Changes in the Catalytic Cycle of DNA Topoisomerases*. Editor(s): Maria Spies, Yann R. Chemla. Methods in Enzymology, *2016*. Volume 581, Pages 317-351.

ISBN: 9780128092675

DOI: https://doi.org/10.1016/bs.mie.2016.08.013

[31] S. Lee, Y. Jang, S.-J. Lee, S. Hohng. *Chapter Fifteen - Single-Molecule Multicolor FRET Assay for Studying Structural Dynamics of Biomolecules*. Editor(s): Maria Spies, Yann R. Chemla. Methods in Enzymology, Academic Press, Vol. 581, *2016*, Pages 461-486.

ISSN 0076-6879, ISBN 9780128092675.

DOI: https://doi.org/10.1016/bs.mie.2016.08.015

[32] Doll F, Hassenrück J, Wittmann V, Zumbusch A. *Intracellular Imaging of Protein-Specific Glycosylation*. Methods Enzymol. *2018*;598:283-319. Epub 2017 Jul 31.

PMID: 29306439.

DOI: 10.1016/bs.mie.2017.06.015.

[33] Jones Garth A., Bradshaw David S. *Resonance Energy Transfer: From Fundamental Theory to Recent Applications*. Frontiers in Physics, Vol. 7, *2019*.

ISSN=2296-424X

DOI=10.3389/fphy.2019.00100

[34] Fred Schaufele, Ignacio Demarco, Richard N. Day. *FRET Imaging in the Wide-Field Microscope*. Editor(s): Ammasi Periasamy, Richard N. Day. Molecular Imaging, American Physiological Society, *2005*. Pages 72-94.

ISBN 9780195177206

DOI: https://doi.org/10.1016/B978-019517720-6.50013-4.

[35] Bültzingslöwen, C. V.. *Development of optical sensors ("optodes") for carbon dioxide and their application to modified atmosphere packaging (MAP).*, (2004).

[36] Berezin, Mikhail Y. and Achilefu, Samuel. *Fluorescence Lifetime Measurements and Biological Imaging*. Chem. Rev. American Chemical Society, Vol. 110, Pages 2641-2684, *2010*.

DOI: 10.1021/CR900343Z

[37] Collins, A. T., Thomaz, M. F., Jorge, M. I. B.. *Luminescence decay time of the 1.945eV centre in type Ib diamond*. Journal of Physics C: Solid State Physics, *1983*. IOP Publishing, Vol. 16, Pages 2177-2181.

[38] Joseph R. Lakowicz. *Principles of Fluorescence Spectroscopy*, 3rd edition. Springer, *2006*.

ISBN 978-0387-31278-1

[39] Becker, W.. *Fluorescence lifetime imaging - techniques and applications*. Journal of Microscopy, Vol. 247, Pages 119-136, *2012*.

DOI: https://doi.org/10.1111/j.1365-2818.2012.03618.x

[40] Wille, Marcel, Doctoral Dissertation, *2017*. *ZnO- und CuI-Nano- und Mikrostrukturen: Laseremission und Komplexer Brechungsindex*. University of Leipzig, Germany.

[41] Raatz, N., Scheuner, C., Pezzagna, S. and Meijer, J. (*2019*), *Investigation of Ion Channeling and Scattering for Single-Ion Implantation with High Spatial Resolution*. Phys. Status Solidi A, 216: 1900528.

DOI: https://doi.org/10.1002/pssa.201900528

[42] J. Küpper. *Anderung des Ladungszustandes von NV-Zentren durch p-i-p Dioden in Diamant*. Universität Leipzig. Fakultät für Physik und Geowissenschaften. Masterarbeit, *2017*.

[43] Excelitas Technologies. *High-Performance Single Photon Counting Modules. SPCM Product Series*. Last visited 08/01/2021.

URL: https://www.excelitas.com/product-category/single-photon-counting-modules

[44] Webb, Robert H.. *Confocal Optical Microscopy*. Reports on Progress in Physics, *1996*. IOP Publishing, Pages 427-471, Vol. 59.

DOI: 10.1088/0034-4885/59/3/003

URL: `http://dx.doi.org/10.1088/0034-4885/59/3/003`

[45] Wilson, T. *Resolution and optical sectioning in the confocal microscope*, *2011*. Journal of Microscopy, Vol. 244, Pages 113-121.

DOI: `https://doi.org/10.1111/j.1365-2818.2011.03549.x`

[46] Nair, Rahul Raveendran, et al. *Fine structure constant defines visual transparency of graphene*. Science 320.5881 (2008): 1308-1308.

List of Figures

List of Tables